NASA SP-65

SPACE TECHNOLOGY

Volume I

SPACECRAFT SYSTEMS

L. H. ABRAHAM
Douglas Aircraft Co., Inc.

Scientific and Technical Information Division 1965
NATIONAL AERONAUTICS AND SPACE ADMINISTRATION
Washington, D.C.

FOR SALE BY THE SUPERINTENDENT OF DOCUMENTS, U.S. GOVERNMENT PRINTING OFFICE
WASHINGTON, D.C., 20402 - PRICE 35 CENTS

Preface

THIS IS THE FIRST of a series of publications prepared as notes for a course in Space Technology, given by the California Institute of Technology (Caltech) in cooperation with the Jet Propulsion Laboratory (JPL) from June 19 to July 31, 1964. The program was sponsored by the National Aeronautics and Space Administration under Grant No. NsG–598 and was taught by engineers from industry, from Caltech, and from JPL. It is planned that the complete set will consist of

Volume I	*Spacecraft Systems* by L. H. ABRAHAM,[1] DOUGLAS AIRCRAFT CO., INC.
Volume II	*Spacecraft Mechanical Engineering* by JAMES L. ADAMS, JPL
Volume III	*Spacecraft Propulsion* by F. E. MARBLE, CALTECH
Volume IV	*Spacecraft Guidance and Control* by J. R. SCHULL, JPL
Volume V	*Telecommunications* by J. J. STIFFLER, JPL

[1] Dr. Abraham, the author of this volume, died June 16, 1964. His part of the Caltech course was taught by another Douglas Aircraft Co. engineer, Mr. Duncan Pitman, who also checked the author's proofs for this publication.

Contents

CHAPTER 1

Historical Preface

THE ASPIRATION TO CONQUER SPACE is probably as old as man himself. It can be identified with his longing for survival or for the possession of supernatural powers. Throughout the ages poets, philosophers, and magicians have been entranced by the notion of attaining the supernatural power of levitation. Writers of the 17th and 18th centuries conceived space flight as a form of escapism or lesson in morality. Cyrano de Bergerac and others in the 17th and 18th centuries used the concept of voyages into space as philosophical and literary pretext.

As the early astronomers began to piece together the true nature of the cosmos, writers, scientists, and philosophers began to envision other planets in terms of their own, inhabited by intelligent beings. The famed scientist Kepler is credited with one of the first imaginative essays on space. His *Somnium* relates a voyage to the Moon or "Levania" by his hero, Duracotus.

Similar tales were produced during the Renaissance and the 17th century. Milton's *Paradise Lost* and Gulliver's third voyage to Laputa both have space travel themes. Cyrano de Bergerac's hero in *The States and Empires of the Sun* travels to the stars without wings, by supernatural powers in an ingenious machine which might be interpreted as using jet propulsion. De Bergerac also toyed with the idea of launchings using gunpowder and fireworks.

Huygens, in his *Cosmotheoros,* in addition to giving us a detailed description of the planet Saturn, also discourses on its inhabitants.

Throughout the 17th and 18th centuries, tales of space travel continued to be expressed as imaginary adventures either contrasting with or consistent with the contemporary world. But even during this period some scientific minds began to contemplate seriously the possibility of space travel. Wilkes, for example, produced a book entitled *The Discovery of a New World* with "a discourse concerning the possibility of a passage thither." This book was first published in 1640 and is considered a remarkable product of its time. In one passage Wilkes theorizes that the Moon's surface is covered with a

pumice-like material. The reasoning leading to this conclusion may be regarded as somewhat devious by modern standards; perhaps, it was just a lucky guess, but nonetheless it was an indication of the author's insight. In another section he conjectures on the composition and distribution of meteoroids in the universe, not an uncommon pastime today. Wilkes was even curious enough to crush and examine a meteorite; this was a remarkable step for his day.

The following excerpt from this book speaks for itself:

> Too bold was he, who in a ship so fraile, first ventured on the treacherous waves to saile. And yet now, how easie a thing is this even to a timorous and cowardly nature? And questionlesse, the invention of some other means for our conveinee to the moon, cannot seem more incredible to us than this did at first to them and therefore we have no just reason to bee discouraged in our hopes of the like sucesse.
>
> Yea, but (you will say) there can be no sailing thither, unless they were true which the poets does but faine that she made her bed in the sea. Wee have not now any Drake or Columbus to undertake the voyage, or any Daedalus to invent a conveince for the ayre.
>
> I answer, though wee have not, yet why may not for ceeding times rayse up some spirits as eminent for new attempts and strange inventions, as any that were before them. Tis the opinion of Kepler, that as soon as the art of flying is found out, some of their nation will make one of the first Colonies, that small transplant into the other world (moon). I suppose his appropriating this preheminence to his own countrymen, may arise from an over partiall affection to them. But yet thus far I agree with him that whenever that art is invented or any other whereby a man be conveyed some twenty miles high, or thereabouts, then tis not altogether impropable that some or other may be sucessefull in this attempt.

The fertile mind of Jules Verne produced the most important scientific novels of the 19th century. His machines were rather naive but he intuitively grasped the fundamental principle that flight to the Moon would not be made as lifting flight. Unfortunately, he considered ballistic projectiles the proper means of a lunar mission rather than rocketry.

But through the ages, while these men were philosophizing and dreaming of space travel, engineers were planning machines, and scientists were developing principles and amassing knowledge by which actual space travel could be achieved.

The origin of the rocket propulsion principle, by which all present day spacecraft are launched, may be traced to Hero of Alexander's aeolipile. The use of rockets or "fire arrows" in the 11th century was referred to by Nu Ching Tsung Tao, and in the early part of the 13th century, the Chinese put rockets to serious use in repulsing the Mongols. In the 16th century one Wan Hoo was killed in a car powered by 47 solid rockets. In the late 15th century, Leonardo da Vinci sketched several devices employing rocket propulsion, and

around 1600, Giovanni de Fontana designed and built a rocket-powered mariue torpedo. In the 18th century the Indians used rockets, probably of Chinese origin, against the British. These rockets, however, were so primitive and unreliable that the development of rocketry was largely ignored, while military engineers turned to ballistic-type projectiles fired from cannons.

Technological advances of the early 20th century opened up new possibilities for rocket development. Among the modern pioneers to realize the potential of rockets were the Russian, Konstantin Tsiolkovskiy, the German, Hermann Oberth, and our own Robert Goddard.

Tsiolkovskiy, as early as 1903, proposed a liquid rocket engine and during his lifetime was instrumental in arousing interest in rocketry in his own country. Oberth, despite considerable criticism and skepticism from fellow scientists, established the foundation of flight mechanics which predicted long range rocketry and space travel. Goddard launched the first liquid propellant rocket on March 16, 1926, which date might well be regarded as the date of conception of the "space age."

The first serious use of rockets as a military weapon occurred in World War II. The German V–2, placed in action in 1944, was too late to play a decisive part in the outcome of that conflict, but it awakened the world to the possibility of the rocket as a weapon. The pursuit of superiority in these weapons was to provide the means for launching space probes, then satellites and, eventually, man into space. Technology was now adequate and mental climate favorable for space travel.

On October 4, 1957 the Soviet Union put into orbit around the Earth the first man-made object. It weighed only 184 pounds, but gave birth to the "space age." The United States followed within a few months by putting Explorer I into orbit. These simple instrument packages orbiting in space were soon to be followed by more complex experiments and eventually by men.

Faced with the reality of space flight, the United States has pressed military weapons such as Jupiter, Thor, Atlas, and Titan into service as space boosters. The Saturn system presently undergoing qualification testing is the first design expressly constructed as a space booster. It is hoped that this system will place the first American astronaut on the Moon.

The Moon landing is only the first step into space, however. For the future, the sky is, literally, the limit.

769-877 O—65——2

CHAPTER 2

System Definition

A SYSTEM is defined as any combination of parts, assemblies, and sets joined together to perform a specific operational function or functions. The process of applying science and technology to the study and planning of a system so that the relationships of various parts of the system and the utilization of various subsystems are fully established, before designs are committed, is known as *systems engineering.* A subsystem is a major functional subassembly or grouping of items or equipment essential to the operational completeness of a system.

SPACECRAFT SYSTEM COMPONENTS

Essentially, a space system consists of the following components:

(1) *Boosters*—These are the rockets used to set the vehicle in motion before other stages take over. Due to the versatility of the national space effort a variety of launch vehicles is available, each differing in launch capability. Table 2.1 gives some of the dimensions and performance data on booster systems in the national inventory.

(2) *Transfer stage*—This stage is used to transfer the vehicle from one trajectory to another. In interplanetary travel it is this device which transfers the vehicle from an orbit of the departure planet to the target planet.

(3) *Spacecraft*—The spacecraft is the vehicle required to perform the mission after injection into the desired trajectory. The spacecraft may be a simple scientific instrument package or a complex manned system.

The Echo satellite is an example of a simple vehicle. It is primarily designed as a passive device whose total mission is to provide a surface that is reflective to radiofrequency energy. Its total structure consists of a balloon made of Mylar film, sandwiched between thin layers of vapor-deposited aluminum. These layers not only rigidize the Mylar, but also provide a reflective surface.

Apollo, on the other hand, is an example of a complex spacecraft, the most complex yet conceived. This vehicle must provide trans-

TABLE 2.1—Specifications of U.S. Space Boosters

[LOX=liquid oxygen; RP=kerosene; UDMH=unsymmetrical dimethylhydrazine; IRFNA=inhibited red fuming nitric acid; LH=liquid hydrogen]

Name	Scout	Delta	Thor-Agena B	Atlas D	Atlas-Agena B	Titan II	Centaur	Saturn C1	Saturn C1B	Saturn C-5
No. stages	4	3	2	1½	2	2	2	2	2	3
Propellants	Solid Solid Solid Solid	LOX/RP UDMH/IRFNA Solid	LOX/RP UDMH/IRFNA	LOX/RP	LOX/RP UDMH/IRFNA	UDMH and hydrazine/ nitrogen tetroxide.	LOX/RP LOX/LH	LOX/RP LOX/LH	LOX/RP LOX/LH	LOX/RP LOX/LH LOX/LH
Thrust (lb)[a] Stage 1 Stage 2 Stage 3 Stage 4	86 000 64 000 23 000 3 000	170 000 7 700 2 800	170 000 16 000	367 000	367 000 16 000	430 000 100 000	367 000 30 000	1.5×10^6 90 000	1.5×10^6 200 000	7.5×10^6 1 000 000 200 000
Max dia (ft)[b]	3.3	8	8	16	16	10	10	21.6	21.6	33.0
Height (ft)[c]	65	88	76	72	91	90	100	125	150	280
Payload orbit (lb)	220[d]	800[e]	16 000[d]	2 700[f]	6 000[d]	6 000	8 500[d]	20 000[d]	32 000[f]	240 000[d]
Payload escape (lb)		130			750		2 300			90 000

[a] At sea level.
[b] Excluding fins.
[c] Excluding spacecraft.
[d] 300 n. mi. orbit.
[e] 350 n. mi. orbit.
[f] 100 n. mi. orbit.

portation and life support for a crew to and from a lunar landing, and then return the crew to Earth.

DESIGN SEQUENCE OF A SPACE SYSTEM

The evolution of a space vehicle design from the mission requirements to the launching pad is shown in figure 2.1. Variations of this flow chart will exist within various organizations, but the design process is generally similar.

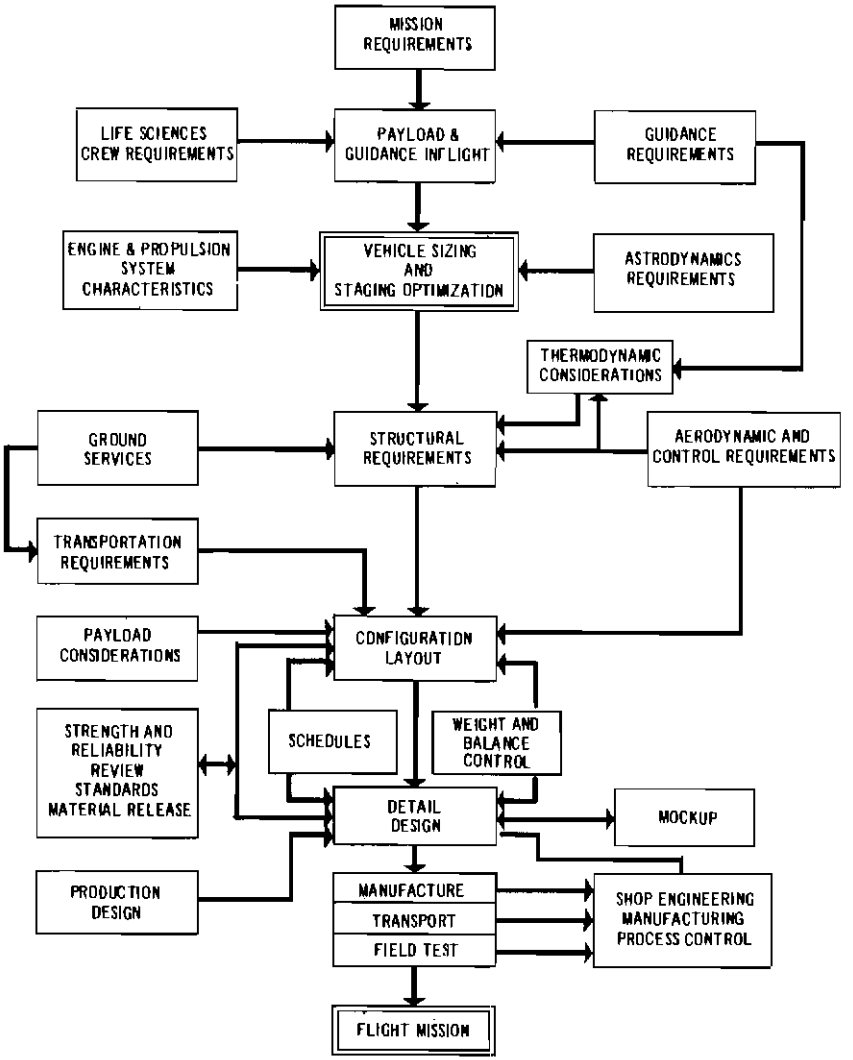

FIGURE 2.1—Vehicle design sequence.

The design and development of even the smallest space vehicle is one of the most complex efforts ever undertaken by man. It requires the coordination and integration of a multitude of scientific and engineering skills along with the most prosaic of the everyday mechanical arts. An aerospace organization employs the skills and knowledge of people ranging from artisan to zoologist and uses such diverse materials as aluminum and zirconium.

The blending of these skills and arts to produce ultimately a device as remarkable as a space vehicle is a considerable achievement.

The development of the vehicle begins with a definition of the basic mission objectives and a range of auxiliary mission envelopes within which the vehicle might be expected to operate. A serious and imaginative approach at this time will produce a vehicle with versatility and growth potential for future missions as well as providing those for immediate use. With the volatility of the space program this versatility cannot be overemphasized.

MISSION REQUIREMENTS

Design effort begins almost concurrently with the definition of the basic mission spectrum and the completion of the operations analysis of the system. The ideal design development consists of a series of overall vehicle system design studies. The first studies naturally can be only conceptual in nature. In this phase, advance state-of-the-art in propulsion, structural design, materials and manufacturing arts is evaluated for advantage and possible incorporation into the design. Decisions made at this time can be most decisive in the lifespan of the system. An overconservative selection of a propellant or the improper selection of construction material will seriously limit the effective life of the vehicle. In the extreme, the design can die aborning.

The main purpose of this sequence of preliminary design studies is to estimate the major characteristics of the vehicle and to define its performance and operational characteristics. At this time, necessary supporting systems are delineated and coordinated. The study will yield the following pertinent data from which the balance of the design may evolve:

(1) Vehicle performance
(2) Payload
(3) Staging optimization
(4) Trajectory shaping
(5) Staging thrust-to-weight (T/W) ratios

At this milestone in the design study, major development problems evolve. The required supporting research programs must now be

considered both as to schedule and risk involved for the entire vehicle system.

STAGING

A sonde, satellite, space probe, or manned spacecraft requires, for the accomplishment of its mission, a specific quantity of kinetic energy. Generally this is expressed in terms of velocity. For example, the velocity necessary to sustain a circular orbit around the Earth is

$$V = r_w \sqrt{\frac{g_a}{h + r_w}}$$

where

r_w = Earth's radius (2.09×10^7 ft)
g_a = gravity at the Earth's surface (32.2 ft/sec^2)
h = altitude of satellite

Thus, to maintain an orbit at 500 000 ft a velocity of 25 700 ft/sec is required.

Since there is no analytical method which allows equations describing a multistage rocket to be solved for the optimum mass ratio of each stage (if the effects of gravity are considered), the solution must be one of iteration. With rocket propulsion, the velocity which may be obtained is dependent on the performance (specific impulse) of the propellant, the quantity of propellant aboard the vehicle, and the weight of the vehicle and payload. The weight breakdown of a typical launch vehicle is roughly:

	%
Propellant (fuel)	88
Propulsion	4
Payload	6
Structures	2

Defining propellant ratio as λ', then

$$\lambda' = \frac{\text{weight of fuel}}{\text{gross weight}}$$

Thus, for a vehicle with a weight distribution as cited above, at the start of burning λ' will be 0.88. As burning progresses, this ratio decreases as shown in table 2.2.

For the case of staging, assume that the fuel is divided between two containers in the ratio of 7 : 3. After the first container is exhausted, it is discarded with the first-stage powerplant and any auxiliary structure. Under these circumstances, the payload will

TABLE 2.2—Change of Propellant Ratio with Burning Time

% Burn Time	Weight, %				
	Fuel	Propulsion	Payload	Structures	λ'
0	88	4.0	6.0	2.0	0.88
10	79	4.4	6.6	2.2	.87
20	70	4.9	7.3	2.4	.85
30	62	5.4	8.1	2.7	.83
40	53	6.2	9.2	3.1	.81
50	44	7.1	10.7	3.6	.79
60	35	8.3	12.4	4.1	.74
70	26	10.4	15.6	5.2	.68
80	18	11.5	17.3	5.8	.60
90	9	19.3	28.9	9.6	.43
100	0	33.3	50.0	16.7	0

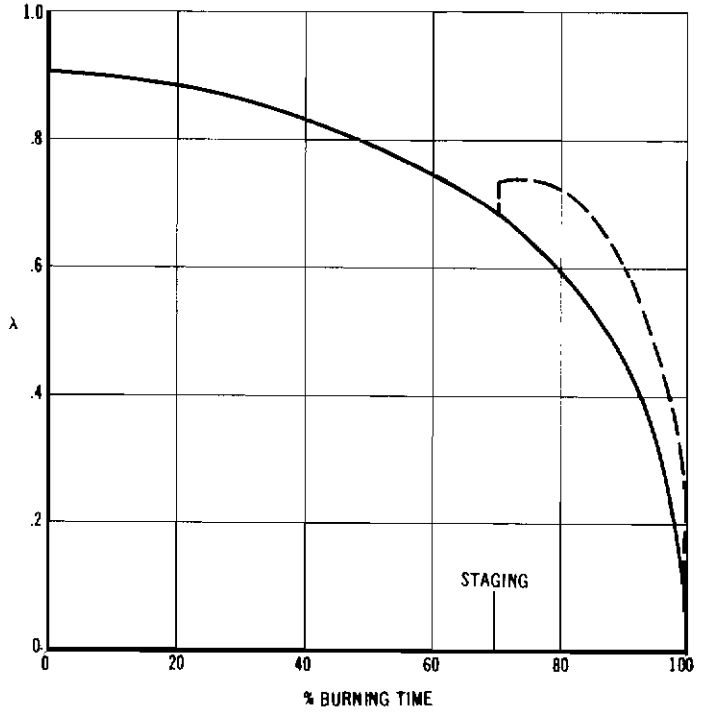

FIGURE 2.2—Effect of staging on λ'.

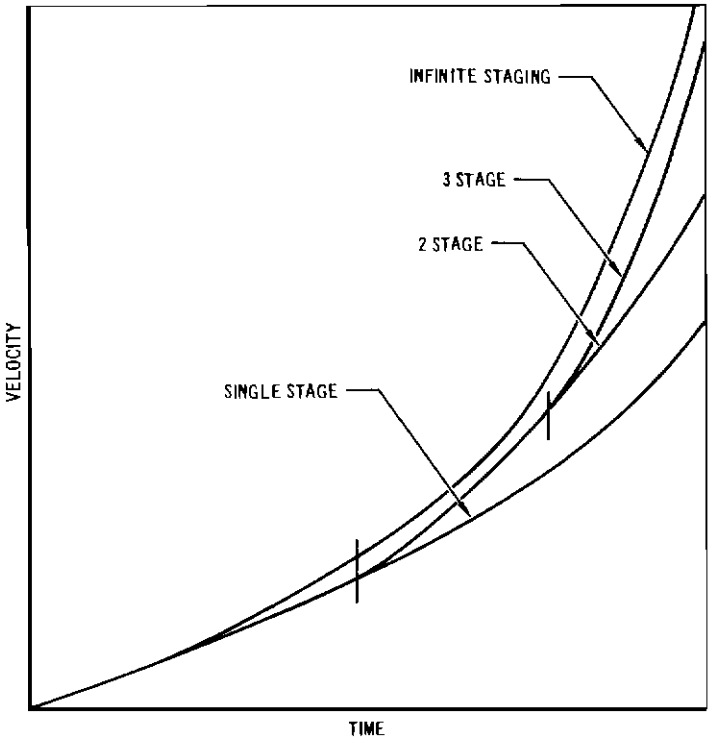

FIGURE 2.3—Effect of staging on burnout velocity of a launch vehicle.

remain constant in weight, but the propulsion system weight as well as the structural weight will decrease. That is, after staging, the weight breakdown might be as follows:

	%
Propellant (fuel)	75
Propulsion	4
Payload	17
Structure	4

After staging the mass fraction would be 0.75 instead of 0.68 as shown in figure 2.2. The effects of staging on velocity are shown in figure 2.3.

Actually, λ' is a measure of the efficiency of the system. The higher λ', the more energy there is available to accelerate the payload. Thus, if the inert structure could be discarded as soon as it is no longer required, the overall efficiency of the system would then be maximum. Dividing the fuel into a number of containers and discarding each as it is emptied would be ideal. In practice, usually only two or three such stages are realistic.

769-377 O—65——3

Launch dynamics considerations usually require a takeoff thrust-to-weight (T/W) ratio of about 1.2 to 1.3:1 (a value as low as 1.1 is acceptable if the wind velocity at launch can be restricted to a low value). This immediately prescribes the engine requirements for the first stage. Second stage T/W ratio is generally influenced by first stage burnout velocity and can vary from 1 to 2 at the lower burnout velocities. Third stage T/W ratio should be of the order of about 1:1 for a multimission vehicle. Optimum last stage T/W ratio shifts widely according to injection conditions, but, except for unusual operations, performance is not greatly affected for a range of values from 0.6:1 to 1.2:1. It must be kept in mind, however, that these factors are not hard and fast and require considerable study to establish the most favorable ratios.

CHAPTER 3

Sizing the Vehicle

THE INCREASING SIZE OF SPACE VEHICLES and the increasing complexity of their missions puts coutinuously greater pressure ou the designer to determine the most efficient design for each vehicle proposed. Before the detail design of the space vehicle can begin, certain overall system studies, as sequenced in figure 2.1, must be completed. The sizing and configuration study which creates a vehicle that will perform the flight mission is a complex procedure. Figure 3.1 illustrates this study process.

In sizing a vehicle, the choice of length and diameter (L/D) ratio is influenced by several parameters. In order to arrive at a minimum structural weight each of these parameters must be taken into accouut and the overall optimum structural configuration evolved. Thus, the influence of dome shape L/D ratio, engine weight, interstage and skirt weight and pressurizing system weight, to mention the most important items, must be evaluated.

Figures 3.2 and 3.3 show the effect of dome shape on the weight of the engine and the interstage and skirt of a given stage. With the shallower dome it is to be expected that a shorter interstage and skirt would be feasible. On the other hand, increased engine weight in the smaller diameters will offset most of this advantage. Then, as shown in figure 3.4, a minimum weight L/D may be determined.

These trade-offs are extremely difficult to handle manually; consequently, most of these evaluations are accomplished by digital computers. The principal purpose of these figures is to emphasize the complexity of the sizing operation and the futility of a manual attempt on anything except tbe simplest design.

Even after these optimizations are accomplished, there must be certain logical perturbation. For example, from a control standpoint it is desirable to keep the diameter as large as possible. If this can be accomplished without undue weight penalty or performance loss, it simplifies the guidance and control system to the extent that phasing networks and body mode accelerometers can be omitted in a very rigid vehicle.

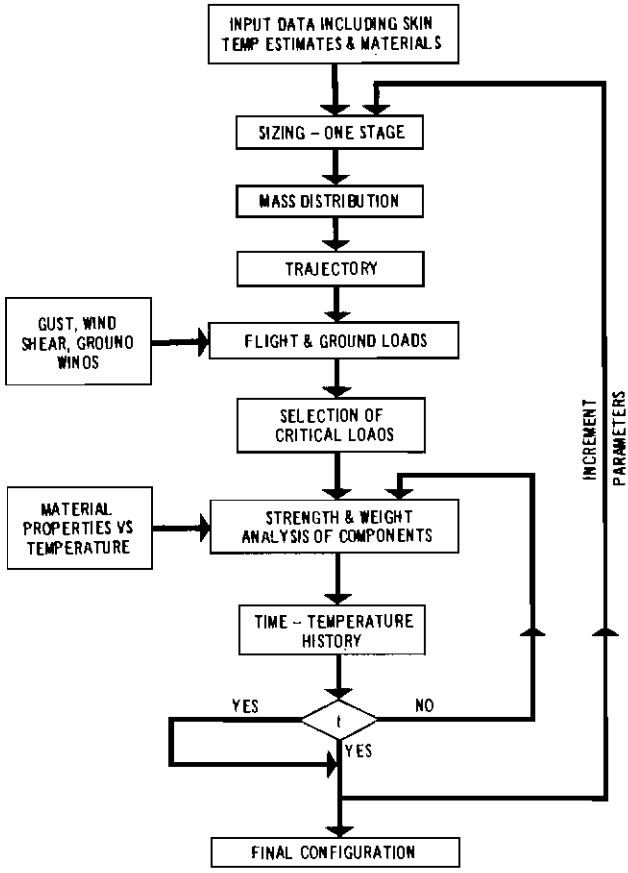

FIGURE 3.1—Flow chart for configuration study.

In general the sizing operation will follow the flow chart shown in figure 3.1 In this process each configuration must, in turn,

(1) Be sized to accomplish the mission
(2) Be flown through its mission profile
(3) Have aerodynamic flight loads and mass distribution data determined on the basis of standard gust wind shear and ground wind criteria
(4) Have critical loads determined
(5) Have preliminary stress analysis performed including temperature effects on materials
(6) Have weight of components computed
(7) Utilizing the newly determined mass distribution, have a new time-temperature history determined
(8) With this new time-temperature history, have structural thicknesses adjusted and recycled until the process converges.

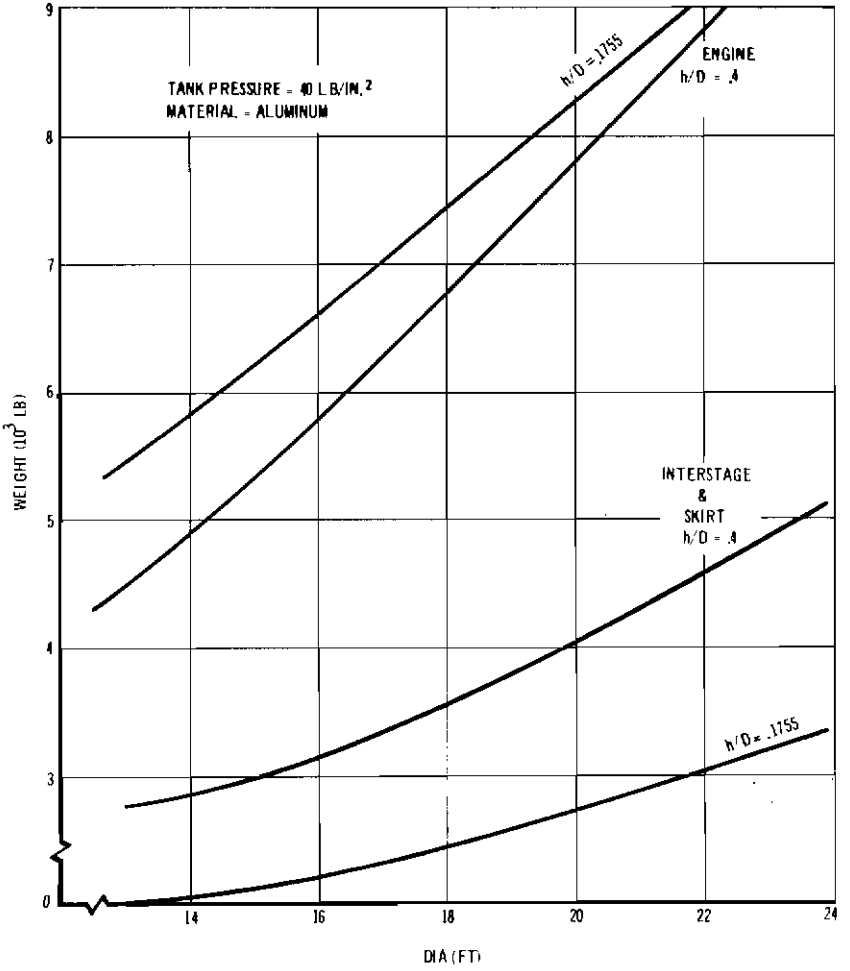

FIGURE 3.2—Effect of dome height on skirt, interstage and engine weight.

Engineering design is an iterative decision-making process. It involves identification of a need and an examination of possible solutions which are tested against recognized criteria of performance. Many repetitions of each step are made in a search for acceptable or, hopefully, optimal results. Each step in each iteration involves choices and decisions. The more information which can be utilized in each decision, the better the decision is likely to be. This information is of two kinds: that which is stored in the designer's mind (experience) and is readily accessible for use, and that which must be acquired.

Usually two or three promising configurations will result from this preliminary design exercise. All of these designs will have merit

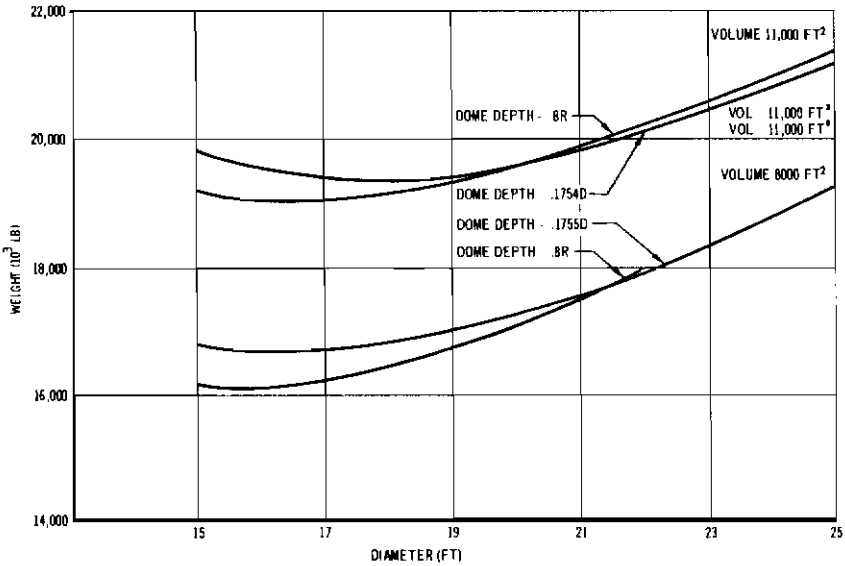

FIGURE 3.3—Effects of dome shape on booster weight. Pressure=20–30 lb/in.²

and only by further study and evaluation will the selection of a single design be possible. Figure 3.5 shows an example of the results of a second stage configuration study. Note the variation in configuration possibilities that provides adequate mission conformity.

Once this selection is made, development and research problems may be pinpointed. Engineering and production schedules are now established and the general sequence of order given in figure 2.1 may be set in motion. The detail design then developes, with the end product being, hopefully, a successful operational vehicle.

A complete multistage vehicle configuration study can be performed with these iterative procedures. Each stage is analyzed in turn until all stages have been evaluated and further iterations fail to produce significant changes in any stage.

Load sources acting on a spacecraft structure may be categorized into two types: static and dynamic. Static loads are of particular use in evolving the preliminary structural design. For this purpose, the structure is considered to act as a rigid body. However, once a preliminary design has been achieved, it is possible and necessary to compute the dynamic characteristics of the structure. With this delineation of the dynamic characteristics, it is now possible to include the effects of the dynamic loads on the system behavior. This implies study of the interactions between the control system, propulsion system, aerodynamic effects, and the dynamic behavior of the structure.

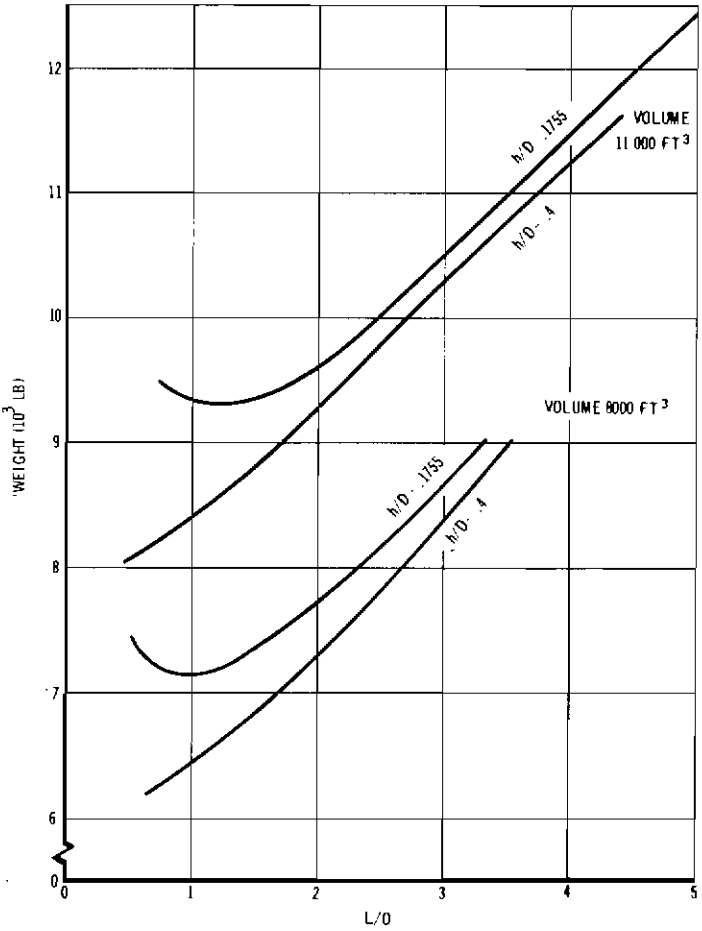

FIGURE 3.4—Effect of L/D and dome height on tank weight. Tank pressure=40 lb/in.^{2} Material=aluminum.

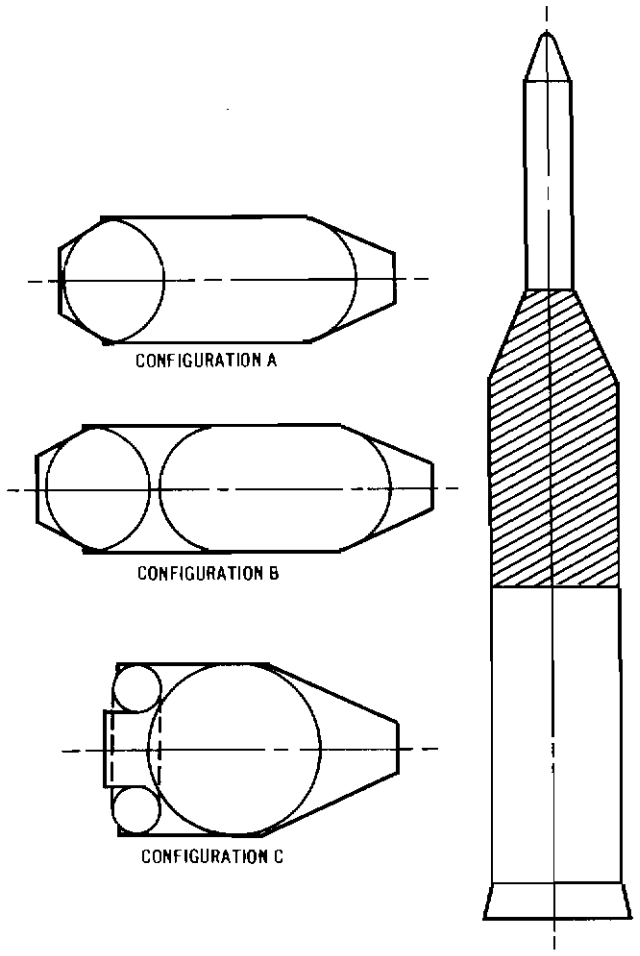

FIGURE 3.5—Example of a second stage configuration study.

CHAPTER 4

Aerodynamic, Powerplant and other Loads

THE COMPONENTS OF A BOOSTER or spacecraft must be designed to survive during manufacturing operations, transportation to the launch site, launch, mission operation, and reentry. In addition, there may be other considerations such as storage or erecting procedures that may impose special loads or environments.

Before the engine is ignited, but while the operational vehicle (boosters and spacecraft) is resting in the launch complex awaiting takeoff, ground winds can induce severe loads both as a steady drag load or as a dynamic response in a direction mainly normal to the wind direction. This latter response, due to vortex shedding, is a low-velocity phenomenon which will occur at a critical velocity that is dependent on the natural frequency of the structure, Reynolds number, placement of protuberances, tunnels, etc. Even the proximity of ground support equipment in the immediate vicinity of the craft can influence the critical velocity and the severity of the oscillation. Figure 4.1 shows an example of the increase in bending moment over a rigid body analysis resulting from vortex shedding.

At engine ignition and release, longitudinal transient loads are generated which can be rather severe not only as they affect the basic structure, but also as they affect smaller components of equipment. The magnitude of these effects is illustrated in figure 4.2. The rigid body analysis would consider only a steady-state thrust force while, actually, the interaction between the thrust transients and the elastic characteristics of the structure would produce an amplification factor of almost 2.

Engine noise is most severe in close proximity to the ground; the noise generated by the engine can be of extremely high intensity. This sound pressure will affect the structure as well as flight or ground service equipment. Considerable attenuation of the sound pressure is often provided by the structure, but in many cases even this attenuation is not sufficient to prevent damage to delicate instruments and equipment.

769-377 O—65——4

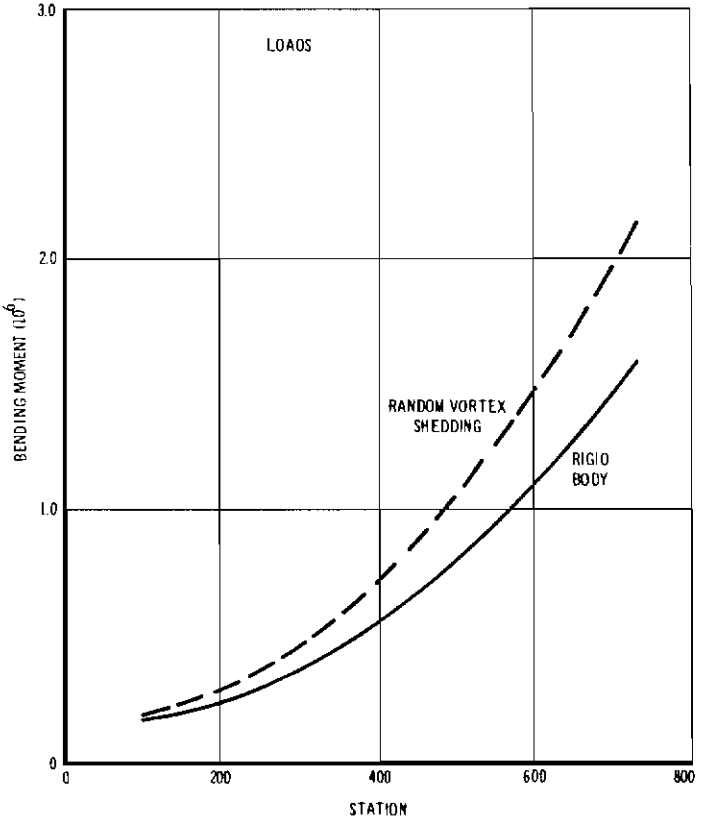

FIGURE 4.1—Ground oscillation effects comparison.

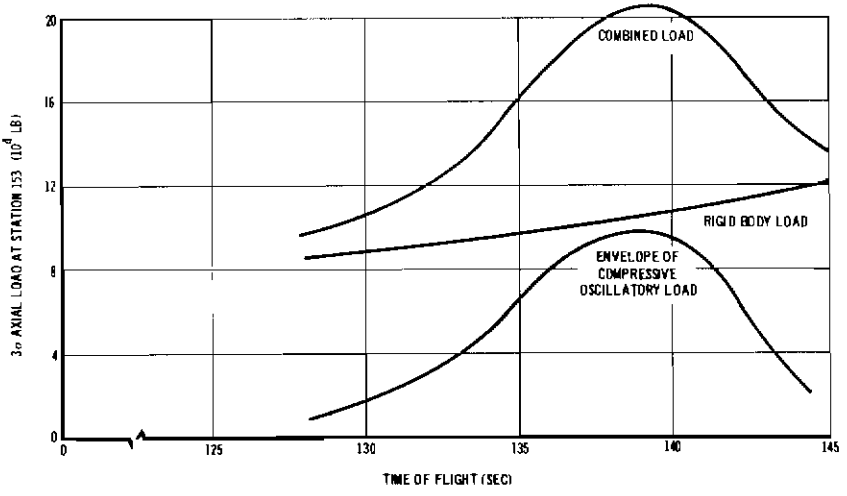

FIGURE 4.2—3σ axial load at station 153 vs time of flight. Boosted weight=17 200.

As the spacecraft leaves the ground, noise diminishes, not only because of the attenuation of reflected noise, but also because of the reduced density of the air and Doppler attenuation. It must be remembered however, that even at supersonic speeds at high altitudes, noise and vibration still can be transmitted by the structure and through fluid columns.

In addition to the engine noise, the following are sources of vibration encountered during the launch phase of the flight:

(1) Engine ignition shock
(2) Thrust pulsation (chugging)
(3) Turbine chugging
(4) Boundary layer noise
(5) Fuel sloshing
(6) Control forces
(7) Nonstationary aerodynamic forces
(8) Unbalance of spinning components
(9) Engine burnout and staging shocks

During flight through the transonic regime to the maximum dynamic pressure region, the thrust and various other local steady-state oscillatory aerodynamic loads become important. In this phase of the flight, the spacecraft may experience transient as well as steady state accelerations resulting from atmospheric winds and wind shears, and from static pressure peaks which appear around geometric discontinuities. These latter peaks are especially aggravating at transonic speeds where they may be superimposed on buffeting loads.

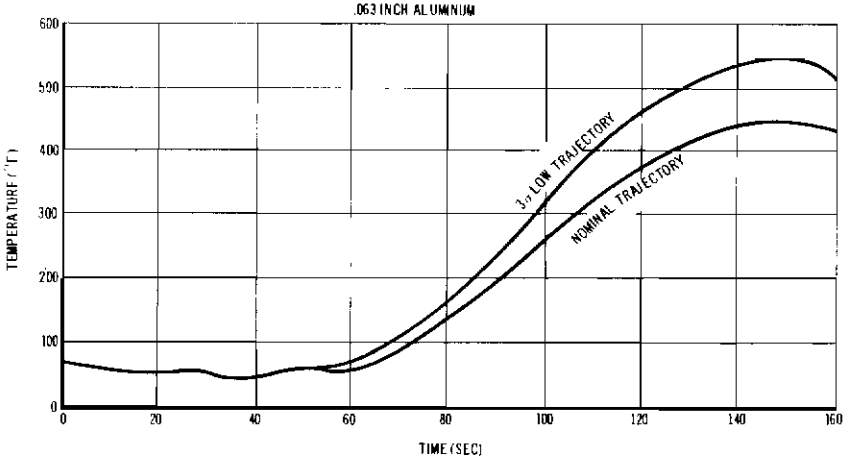

FIGURE 4.3—Temperature history of the transition section.

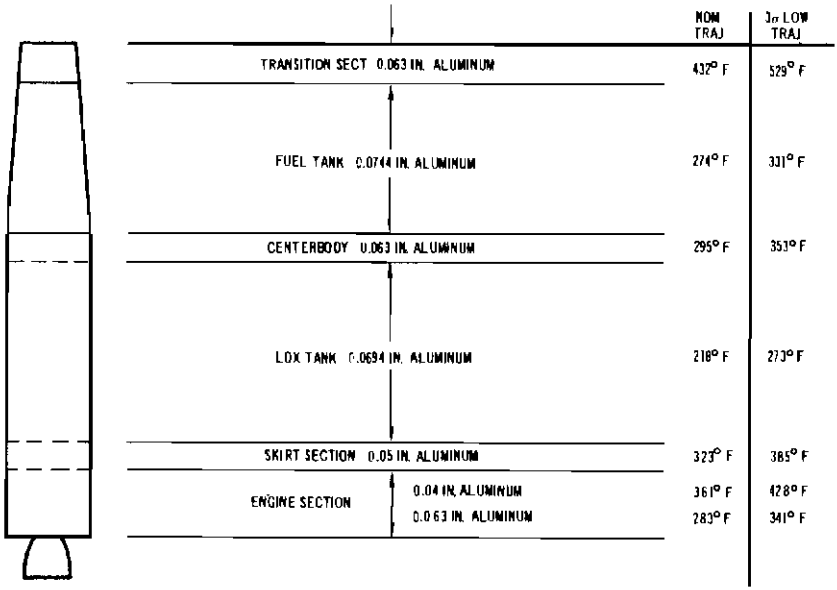

FIGURE 4.4—Maximum temperatures of A–12 trajectory.

In this same flight regime, consideration must he given to the control of the vehicle. This aspect, as well as stability and the coupling of the control sensors with the vehicle flexibility modes, must be considered in making any necessary corrections. Fuel sloshing can be an additional aggravation during transonic flight.

Flutter of aerodynamic surfaces, such as fins, will generally be critical in the transonic maximum-dynamic-pressure regime. Thin, large, unsupported panels may also pose a flutter problem.

As the spacecraft rises in altitude, the exhaust plume of the engine will widen as the atmospheric pressure is decreased. This increase in plume size and radiation can cause severe heating problems at the base of the structure.

Another serious, and often neglected, consideration in vehicle design is trajectory variation. This can result from many sources but it is sufficient to state here that a realistic tolerance must be placed on a trajectory and the ramifications of these tolerances must be considered. Figure 4.3 reflects the variation in temperature due to the flight trajectory being on the low side. Without previous consideration this effect could have caused a structural failure. Figure 4.4 shows these maximum effects on various sections of a Thor booster.

CHAPTER 5

Material Selection

IN SELECTING THE PROPER STRUCTURAL MATERIALS for a space vehicle booster the three most important problem areas which must be considered are:

(1) *The environment:* The natural and operational environment to which the material will be exposed must be understood and the combined effects as well as the individual effects on the material must be studied

(2) *Material properties:* In general, the physical and mechanical properties of most materials are readily available. If, on the other hand, better materials are required to cope with the environment or the special loadings of a given mission, a better understanding of both the nature and origin of these properties will often yield a more desirable solution. This understanding may go so far as an understanding of such details as molecular interactions which affect the engineering properties of the material. For example, molecular dislocations may cause fracturing, or radiation effects may cause breaking of long-chain molecules in elastomers. Such mutation could result in embrittlement or loss of elasticity of the material

(3) *Application to design:* The application of a material to a design will offer basic considerations whereby a thorough and basic understanding of physical phenomena could remove certain physical limitations imposed on a material. Ablative cooling is a prime example of such ingenuity. Cathodic protection against corrosion is another example

ENVIRONMENTAL EFFECTS ON MATERIALS

The structure of a booster or space vehicle represents a most unique and unusual integration of materials and environment. With the possible exception of the nuclear powerplant, no other device can approach this claim to complexity. The unique aspects of the space

environment which must be considered in any material selection are:

(1) Vacuum
(2) Particles
(3) Meteoroids
(4) Operating temperatures

In addition, the following criteria have a direct bearing on the selection of a material:

(1) Economics of the complete vehicle
(2) Strength-weight ratio
(3) Experience in design and fabrication of the material
(4) General state-of-the-art for production and fabrication
(5) Temperature behavior characteristics
(6) Physical characteristics when in contact with propellants
(7) Available insulations and bonding techniques

Vacuum Effects

The operation of a space vehicle may involve exposure to the hard vacuum of space for extended periods of months or years rather than minutes and seconds. The first implication of this extended vacuum exposure is the loss of material that may result from evaporation or sublimation. In general, this loss will be insignificant in its effect on the load-carrying ability of metallic elements. This will be true for most metallic materials even at moderate temperatures. This material erosion, however, will not be insignificant where thin coatings are used for thermal control or other purposes. Sublimation can be a very serious problem where very thin coatings are used to control the emissivity or absorptivity characteristics of a surface. With very thin coatings, the loss of a thickness of only a few angstrom units can change its sensitivity spectrum. Figure 5.1 shows the effects of prolonged vacuum exposure on several coatings used for radiators. These tests were performed in a vacuum at a temperature commensurate with the operating temperature of a radiator.

Friction and wear of a moving surface is both a mechanical and chemical process. Most systems are heavily dependent on physiochemical barriers for the prevention of welding between the microscopic roughnesses of the moving surfaces. These barriers are usually reinforced by the assistance of a film of fluid lubricant which is hydrodynamically established and maintained.

In the absence of air pressure, liquid lubricants will generally evaporate. A low-vapor-pressure fluid can be used with a moderate life expectancy, but where high temperatures and a long service life are expected, even low-vapor-pressure fluids are not totally satisfactory. For this application solid lubricants must be substituted.

With a solid lubricant, the faying surfaces are separated by a low-vapor-pressure solid film. Such films are not self-replenishing, and their effective service lives are limited. Even ball or roller bearings are subject to some sliding action which will wear away solid films. Once the vacuum environment of space causes this protective lubricating film to break down, the contact surfaces become "clean," and surface particles begin to weld so that the bearing soon becomes rough or even freezes.

Many dry-rubbing components depend on absorbed lubricants to reduce friction; even a material such as steel is lubricated by its oxide surface coating. Once this coating is broken under vacuum conditions where it cannot be replaced, the frictional forces will increase greatly and under certain pressures the surfaces will weld. This action is, of course, accelerated by increases in temperature and/or pressure. Thus, in the space environment, spacecraft doors can weld shut, relay contacts stick, or switches freeze.

Particle Radiation Effects

While only a few failures can be attributed to the vacuum environment, there have been several failures of spacecraft that can be attributed directly to particle radiation. Particle radiation in space may be divided into three categories: solar flare particles, cosmic radiation, and trapped radiation. The primary galactic radiation

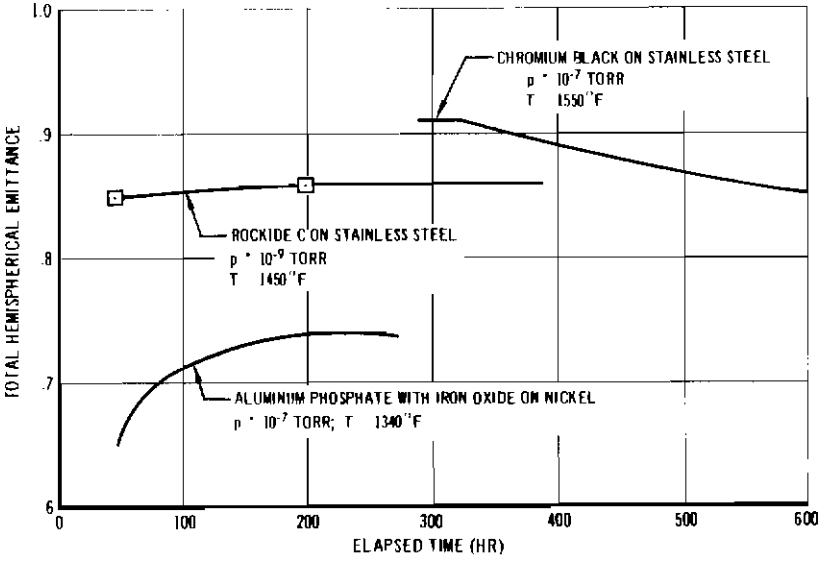

FIGURE 5.1—Effects of vacuum on total hemispherical emittance at elevated temperatures.

consists of positively charged particles of very high energy. But even for man—the most radiation-sensitive material with the possible exception of photographic plates—this radiation may be negligible except after many years of exposure. The energy spectrum of the other major constituents of space radiation is such, however, that radiation-induced changes in the materials can be caused by ionization and excitation processes. The coupling of these effects with the vacuum environment will produce effects not necessarily predicted by the addition of effects of tests performed by separate exposures.

Organic compounds, which include the man in the system, are very susceptible to the inonization and excitation processes. The mutation is generally proportional to the total integrated dose received, regardless of the type or quantity of the radiation. Thus, the solar flare may present problems for some of the more sensitive materials but because of the sporadic nature of these flares the time-averaged flux will be relatively light. Light weight shielding will suffice for protection of most materials from this source. Protection of the hypersensitive occupants, however, will require some other form of effective shielding. Improved effectiveness of passive shielding in the form of an active magnetic shield or a heavy passive shielding in which the occupants may shelter during an outburst may be developed. Refinements in prediction of solar flares would make flight postponement or cancellation possible.

Within the Van Allen belts, the dose rate experienced due to trapped radiation will be high enough to affect any organic compounds used in the spacecraft structure. However, most organic structural materials require large doses of such radiation before macrochanges occur, so long-exposure protection from this radiation may be obtained with very light shielding.

However, it may not be easy to devise adequate shielding for some items. For instance, solar cells operate by radiation to which they are particularly sensitive. Shielding for solar cells and for other light-sensitive or optical systems must remain transparent even under radiation. Most glasses discolor under radiation and as yet there is no adequate solution for this problem.

The principal emanations from nuclear fission are:

(1) Alpha particles
(2) Beta particles
(3) Fast neutrons
(4) Gamma rays

The radiations of principal concern to the spacecraft structure will be the fast neutrons and the gamma rays. The fast neutrons inflict damage by what is essentially a collision process. Gamma rays, on the other hand, are of an electromagnetic nature and produce

damage by an ionization process. Damage by Gamma radiation causes impurities and interstitials within the construction material, and may also create atomic vacancies and thermal spikes.

Metals and ceramics are mainly affected by neutron radiation which tends to destroy their orderly structural arrangement. Other materials may be mutated by the destruction of chemical bonds, creation of free radicals, out-gassing, cross-linking, and polymerization. Naturally, these changes in composition and structure must be accompanied by dimensional changes. Of all the materials, metals are the least susceptible to this type of damage while organic compounds, including man, are most susceptible. Plastics and elastomers, as a class, are also quite susceptible to radiation damage. Figure 5.2 illustrates the effect of out-gassing time on fatigue life.

Meteoroid Protection

Certainly damage to a spacecraft which would endanger the occupants or prevent fulfillment of the mission must be avoided. The hazard presented by meteoroid strikes is a difficult problem for the space system designer because of the many uncertainties in the size, composition, weight, flux density, and velocity of meteoroid particles. Even the penetration mechanisms are not well understood, and simulation of the high end of the velocity scale is very difficult.

Considerable effort has been devoted to systems designed for meteoroid protection. One of the most promising devices is the meteoroid

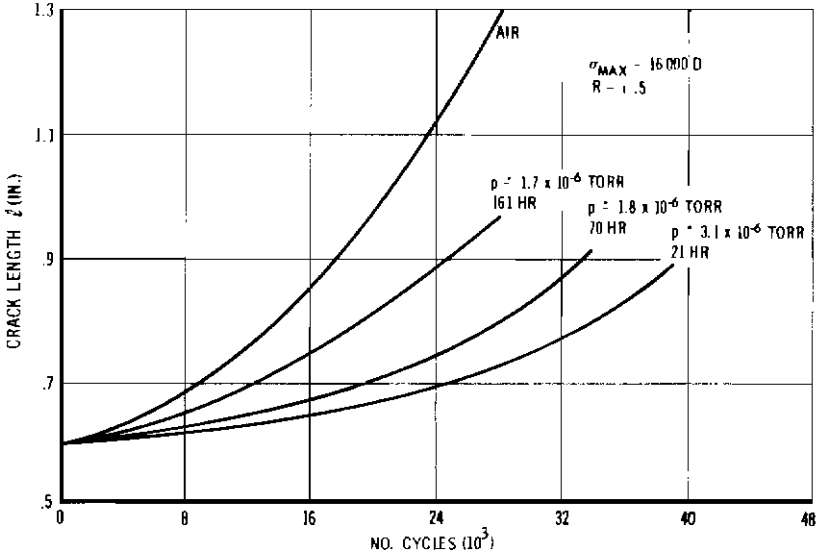

FIGURE 5.2—Effect of out-gassing time on fatigue life.

769-377 O—65——5

bumper. This protection consists simply of a thin sheet of material that is placed in front of the primary structure and at some distance from it. In general, material selection plays little part in the protection of structures from meteoroid particles. The primary parameters here are those of geometry and the physical properties of the materials have only small effects. Where the effects of the damage must be assessed, however, the problem is definitely one of material characteristics such as fracture toughness.

Many of the physical properties of titanium, steel, stainless steel, and aluminum alloy systems are reasonably constant. For instance, all titanium alloys possess almost equal elastic moduli, density, coefficient of thermal expansion, specific heat, and conductivity. This is also generally true for aluminum and precipitation-hardenable stainless steel alloys. As a result, the designer can easily choose between these alloy classes, if physical properties are an important consideration in the vehicle design. The problem then is reduced to finding the best alloy in a given base metal system.

The physical properties of most materials are well documented. The mechanical properties that affect the strength of a material strongly influence its selection for a particular application. These particular properties are defined by suitable mechanical tests at the appropriate operating temperature of the structure and are generally available in the literature. Tensile or compressive stress-strain curves usually define these members for the designer, and accurate reproducible test techniques to determine these properties are well established. A typical full-range stress-strain curve with the significant properties derived is shown in figure 5.3.

BIAXIAL BEHAVIOR

If the material under consideration is homogeneous and isotropic, the designer can estimate accurately the stress-strain curve under varying biaxial fields using the distortion energy theory (the von Mises criterion) as shown in figure 5.4. However, those alloys which exhibit a hexagonal close-packed crystallographic structure are generally not isotropic in sheet or flat-rolled form. This anisotropy is known as texturing. The majority of titanium alloys exhibit hexagonal close-packed crystallographic structure, and as a result do not conform to the von Mises criterion. Thus, titanium materials which tend to have strong crystallographic orientation show significant differences in biaxial behavior when compared to isotropic materials. Figure 5.4 also shows a schematic plot of the yield surface in the biaxial tension quadrant. Note the significant increase in yield strength as the degree of thickness anisotropy increases. Figure

5.5 compares the uniaxial, predicted biaxial and actual biaxial curves for a pressure vessel of titanium alloy (Ti-6Al-4V).

FRACTURE TOUGHNESS

Toughness (fracture toughness) is a particular mechanical property that defines the load-carrying capacity of a material in the presence of a flaw.

A flaw is a material defect such as a crack which runs only partially through the thickness of the material and usually results in plane strain (triaxial stress) at the front of the flaw. Load-carrying capacity

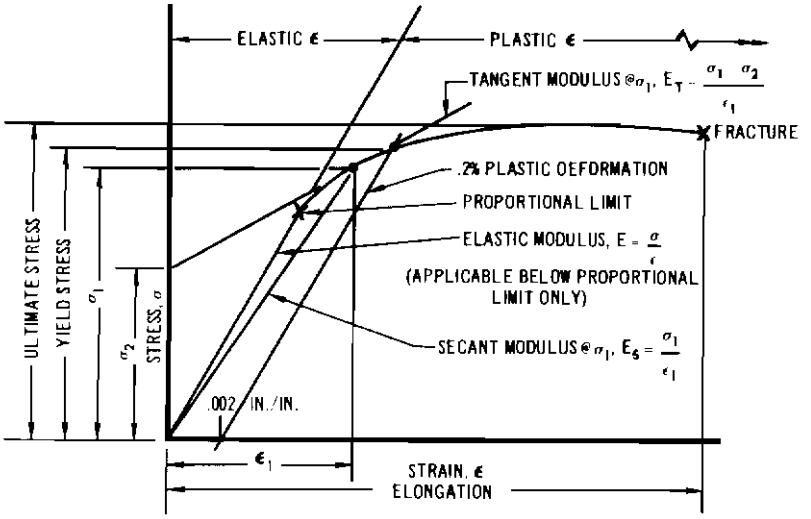

FIGURE 5.3—Typical full-range stress-strain curve showing significant design features.

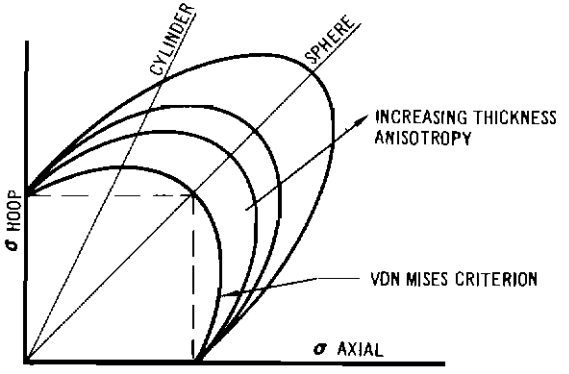

FIGURE 5.4—Yield surfaces in biaxial tension for textured materials.

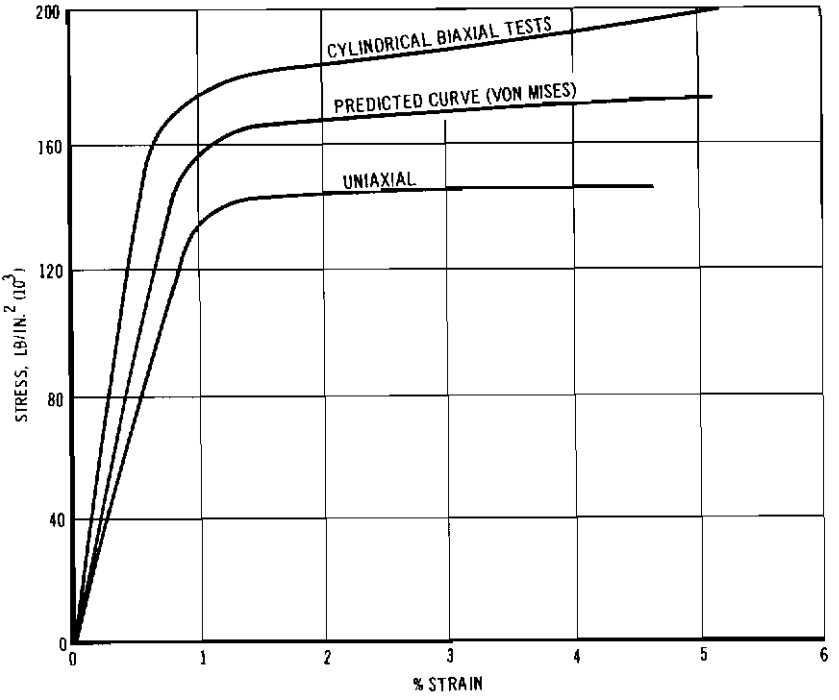

FIGURE 5.5—Stress-strain behavior for anisotropic titanium. (16 in. diam test cylinder of Ti-6Al-4V.)

is the gross or net fracture stress that a material will carry in the presence of a flaw. Net fracture stress is the maximum load divided by the total cross section area including the flaw area. A critical flaw size is the largest flaw a material can withstand before its load-carrying capacity falls below its ultimate tensile strength.

The most common type of flaw found in pressure vessels is a crack in or near a weld zone that penetrates only partially through the thickness of the material. It has also been found that data from uniaxial test specimens with shallow cracks induced by fatigue correlate with the results of actual pressure vessel burst tests. Because of this correlation, partial-thickness-crack specimens can be used in choosing pressure vessel materials.

These test results also have direct value for the designer and the nondestructive test specialist. That is, this test quantitatively evaluates materials in a manner that has direct usefulness. Figure 5.6 covers two candidate materials for a pressure vessel. Material *A* is significantly stronger than material *B* but has a critical flaw size that is approximately 0.015 in. deep. On the other hand, material *B*, while somewhat weaker than material *A*, has a critical flaw size approxi-

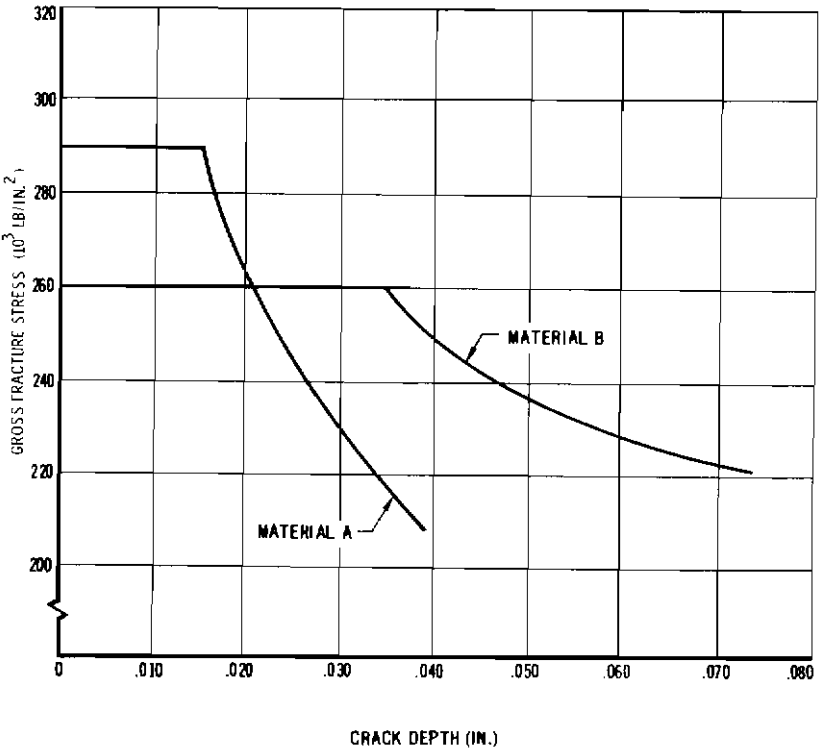

FIGURE 5.6—Material selection based on fracture toughness.

mately 0.035 in. deep. If ultimate tensile strength were the only consideration, material *A* would be the material selected. However, if the nondestructive test specialist could not detect a flaw smaller than 0.025 in. deep with the inspection methods at his disposal, any structure designed from material *A* would be unreliable unless the maximum design stress were lowered. On the other hand, material *B* would be completely reliable, since flaws less than critical size could be detected. Under normal circumstances material *B* would be selected for the pressure vessel since it possesses the maximum attainable strength and reliability. If the designer found that material *B* did not provide structural efficiency high enough to meet the performance requirements, the problem would have to be resolved by the development of a more advanced detection technique which, if such a technique were possible, would generally be more expensive.

CHAPTER 6

Design of Manned Space Cabins

THE DESIGN OF A "SHIRT-SLEEVE" CABIN for a space trip or for the inhabitants of a space laboratory requires a range of cabin pressures from a minimum of approximately 7 lb/in.^{2} to a normal maximum close to atmospheric pressure (14.7 lb/in.^{2}). With the cabin so pressurized considerable emphasis must be placed on preventing inadvertent decompression of the crew compartments. Compartmentation of the working area gives an added safety factor, but in the final analysis the reliability of the individual compartments must be examined closely and made individually safe.

BASIC FAILURE MODES

All of the possible modes of failure are essentially the same differing only in degree. The three basic failure modes whereby compartments may become decompressed are: explosive decompression, fast leak, and slow leak.

Explosive decompression is initiated by a crack or flaw in the pressure-compartment structure which, after reaching a "critical crack length," will become unstable and propagate rapidly. Cracks at, or exceeding, this critical crack length become "fast-cracks" since energy is absolved in the spontaneous running of the crack. In a manned compartment this mode of failure would in all probability kill the occupants instantly, and for all practical purposes it would destroy the shell's geometry rendering the vehicle irreparable.

Before a crack reaches the critical length a rapid leak would probably occur and forewarn the occupants of impending danger. This presupposes, however, that the initial crack is not of critical length. The energy stored in the pressurized compartment would be released at a rapid rate in the event of a fast leak, but not so rapid as to cause secondary damage as in the case of explosive decompression. The compartment bleed-down, however, may be so rapid that the crew may be unable to take timely survival action such as donning pressure suits or retreating to and sealing off a nondamaged compartment. Hence, this mode of failure could be fatal to the entrapped crew members, even though the vehicle could be repaired by the surviving crew.

The slow leak is probably the only tolerable pressure failure. Corrective action can be taken as long as the bleed-down rate is rather slow and location and repair of the damage is possible. But even so, this mode of failure must be considered serious enough to abort a mission and cause an economic or mission penalty ranging from a moderate increase in operating cost to the complete abandonment of the vehicle.

The critical crack length (l) which a panel can sustain and still remain stable, is dependent on the ratio of the residual stress in a panel of width (w) after a crack has appeared (σ_R), to the ultimate strength of the parent material (σ_{ult}). That is

$$\frac{\sigma_R}{\sigma_{ult}} = \frac{1-\frac{l}{w}}{\sqrt{1+\frac{3l}{R_p}}}$$

where R_p is an empirical material factor which varies with the material itself. For aluminum this factor is 13.

POSSIBLE SOURCES AND SIZES OF FLAWS AND DAMAGE

In order to completely define a fracture-safe design, a more thorough study of the sources and causes of cracks and imperfections is necessary. Undetectable manufacturing defects, operational accidents and adverse environmental occurrences are all possible sources of such flaws.

In manufacturing, inclusions of foreign substances can occur in rolled sheet and plate material. These inclusions are sometimes impossible to detect even with sonic, X-ray, or other nondestructive test techniques. These undetected flaws as well as faulty welded joints can start cracks. Weld joints are usually minutely inspected and checked for leaks, but even so, some flaws of this type are not detectable. In areas of "high-flaw risk" the local stress is generally maintained at a much lower level than the rest of the structure to minimize the effects of such imperfections.

Other flaws such as dents, nicks, and scratches occur in fabrication and handling and create a most frustrating problem. In general, these stress risers are burnished or polished out but the possibility of latent damage always exists.

A pilot error or an operational failure of the propulsion control, or guidance system, in a docking-ferry-resupply craft can cause a collision resulting in a puncture of a pressurized compartment of the spacecraft. Most docking criteria specify a relative axial velocity

of about 2 ft/sec and a lateral velocity of about 1 ft/sec. However, even these relatively low velocities can cause considerable collision shock and any accidental contact could cause damage.

Crew accidents may be responsible for other damage. A tool that slips could cause a small puncture and leak and, depending on the working stress of the wall, even a small puncture could precipitate an explosive decompression. Failures of rotating machinery, such as centrifuges and gyros, could also cause punctures of pressurized compartments.

The primary factors governing critical crack growths are: pressure, compartment geometry, material, and operating stress level. Nearly all of the data accumulated so far concerning the critical crack lengths of structural materials have been arrived at empirically. Available data show the critical crack length to be somewhat dependent on form (i.e., geometry) even for identical materials and operating stresses.

For flat plates of various materials under uniaxial loads enough data have been generated to determine the envelope of critical crack length as a function of operating stress or residual strength. Sufficient data do not exist, however, to define the envelope critical crack length for hiaxially loaded elements. The best available data indicate that biaxial stresses are the more critical.

Although information concerning fracture mechanics is accumulating rapidly, the state-of-the-art of this technology does not meet the needs of current design problems. In view of the lack of knowledge concerning the catastrophic nature of failure due to cracking, it is necessary to approach this solution in a conservative manner to ensure the structural integrity of the vehicle and the safety of the occupants. Transport aircraft represent the only source of manned flight operational experience, relative to structural failure. Table 6.1 summarizes cabin design philosophy concerning operating stress levels for several current and proven aircraft. It is true that aircraft cabins are subject to severe cyclical pressure loading, which is quite different from spacecraft cabin loading, but it must also be pointed out that a transport aircraft cabin can suffer a large tear and ensuing rapid decompression without catastrophic results. It must also be emphasized that the proven reliability of aircraft cabin design is attributable only in part to the operating stress level. The attention given to detail in design practices and provisions for a fail-safe structure are very significant factors.

The best available information from past fail-safe design practice and experimental data recommend an *equivalent fracture factor* of 4.0 for a manned space cabin. This is believed to be commensurate with the complexities and unknowns involved in a long-term space

769-377 O—65——6

TABLE 6.1—Summary of Some Ratios of Ultimate Strength to Working Stress for Current Aircraft Pressure Cabins*

Item	DC–6	DC–6B; DC–7	DC–7C	DC–8		Comet I	Comet IV
Aluminum alloy	7075	7075	7075	7075	2014	(*)	(*)
Hoop tension stress at limit cabin pressure, lb/in.^{2}	10 350	13 550	10 650	*8500	13 600	18 350	13 700
Approximate material tensile ultimate stress (corrected for net area effect), lb/in.^{2}	62 000	62 000	62 000	62 000	58 000	*55 000	*55 000
Ratio of tensile ultimate stress to hoop tension (working) stress	*6.00	*4.57	*5.82	*7.30	4.26	3.00	4.01

NOTES: The reader is cautioned to use discretion in comparing these stress ratio numbers. It is stressed that besides working stress, good detail design practice and the provision of fail-safe structure are very significant factors in fracture safe design. In the table, figures for Comet I can only be considered with those of Comet IV assuming (*) the material is the same in the two airplanes. In comparing the Douglas airplanes, a comparison of stress ratios is indicated for parts of one aluminum alloy, 7075, making them compatible. The DC–8 has two alloys in the pressure cabin, 2014 and 7075. The highest stresses for each are listed in the above table. The higher stress level of 2014 reflects the value of the more fracture resistant material of the two. (*) the stress ratio of 2014 for the DC–8 is presented in the table so that the reader may compare it to the stress ratio recommended for space cabin design.

mission. This equivalent fracture factor represents the allowable tensile stress of the pressurized compartment structural material, divided by the maximum permissible stress at the limit operating pressure.

A proof pressure of 1.33 $\times$ the limit pressure is used for proof testing of all commercial aircraft. This pressure will adequately detect leaks arising from structural deflection around seals and manufacturing defects associated with the installation of these seals. In addition, a criterion of an ultimate factor of 2.0 on the limit pressure for the external walls of the cabin is required. The significance of these proof and ultimate pressures, however, is overshadowed by the equivalent fracture factor of 4.0 for fracture-safe design.

It should be noted that structural components, formed by pressure, but not subject to explosive decompression considerations, are designed for ultimate pressure. Examples of this type of structure are frames and sandwich bulkhead faces.

CHAPTER 7

Propellant Tank Design

OPTIMUM DESIGN

THE PROPELLANT TANKS of a booster or spacecraft are generally designed to serve two functions: (1) as pressure vessels and (2) as structural members of the booster or spacecraft, for which the tanks must resist thrust, shear, and bending moment. As pressure vessels, the main stresses encountered by the tanks are hoop stress

$$\sigma_{hoop}=\frac{pR}{t}$$

and axial stress

$$\sigma_{axial}=\frac{pR}{2t}$$

Thus, for any given pressure, the wall thickness will be directly proportional to the pressure. This is shown as the pressure thickness line in figure 7.1. The stress due only to thrust acting on the body is

$$\sigma_A=\frac{T}{2\pi Rt}$$

The stress due to bending is

$$\sigma_b=\frac{MR}{\pi R^3 t}=\frac{M}{\pi R^2 t}$$

Thus, the maximum compression stress on the vessel wall may be written

$$\sigma_{max}=\frac{pR}{2t}-\frac{T}{2\pi Rt}-\frac{M}{\pi R^2 T}$$

The pressure at which all the compressive stresses are balanced out (neutral pressure) is then

$$\frac{pR}{2t}=\frac{T}{2\pi Rt}+\frac{M}{\pi R^2 t}$$

$$\frac{p}{2}=\frac{1}{\pi R^2}\left(\frac{T}{2}+\frac{M}{R}\right)$$

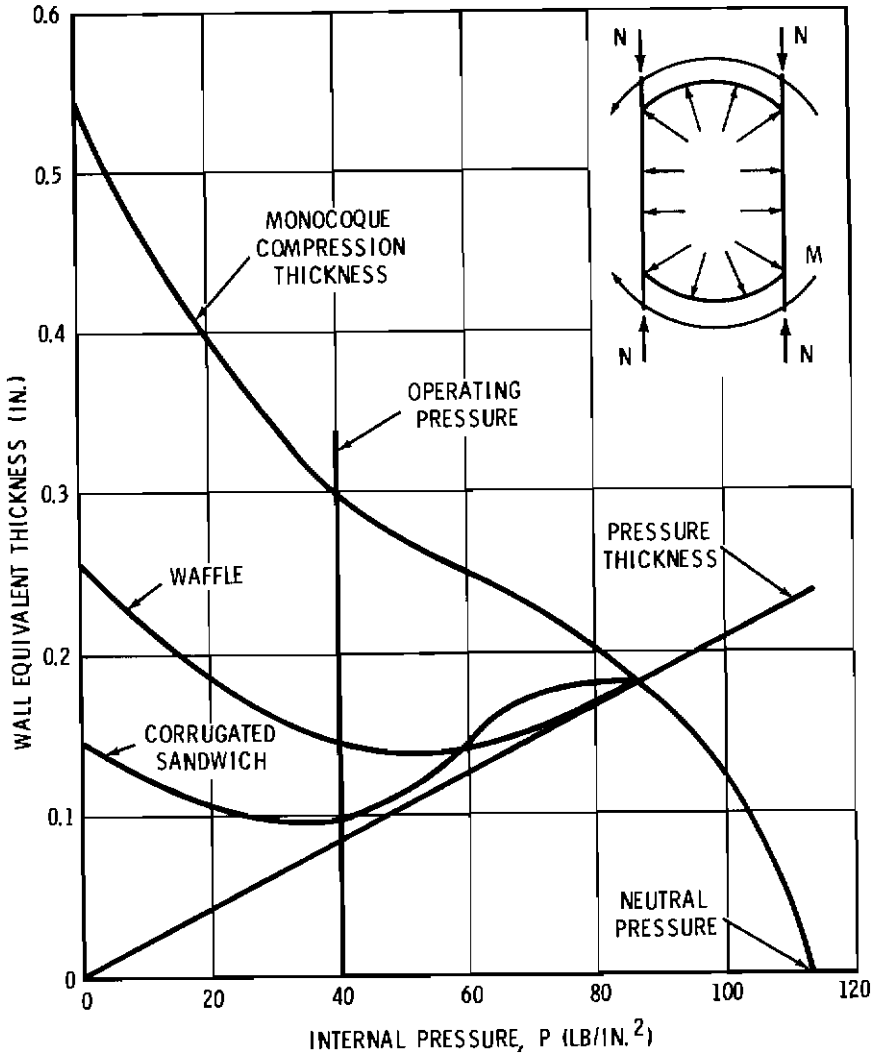

FIGURE 7.1—Advantage of sandwich structure for a large diameter liquid space booster.

Thus, for any given thrust, bending moment, and pressure, there is a thickness requirement for the vessel wall. This thickness required is shown as the monocoque compression thickness curve in figure 7.1.

An examination of figure 7.1 reveals the intersection of the thickness required for pressure and the thickness required for compression stability at a single value of pressure. If this pressure corresponded to the operating pressure of the system, this design would be optimum. Further examination of figure 7.1 reveals that, for an operating pressure

less than the pressure at the intersection of the pressure thickness and stability thickness curves, the vessel would be operating at a very low hoop tensile stress. This design then would be compression critical. Likewise, for any greater pressure, the hoop stresses in the vessel would be high or the vessel would be tension critical. In this case, an improvement in the tensile strength-weight ratio of the material would provide a more effective design.

It can be readily observed that, depending on the bending moment and the internal pressure, different methods of pressure vessel construction will be required to achieve maximum efficiency. As described earlier, figure 5.3 shows the areas in which various construction techniques are most efficient for a pressurized cylinder under thrust, bending, and internal pressure. For high internal pressures (such as those occurring in a solid propellant vessel), a filament-wound structure with its high tensile strength-weight ratio would be most efficient, provided that the bending moment is not too high. If the bending moment is too high, an isotropic wall structure is preferable. For vessels of lower pressures or interstages where the pressure is zero, truss-core sandwich and honeycomb structures are clearly superior except in the very high bending moment regime. These generalizations, as shown in figure 7.2, are supported by existing design practices. Of course, there are other considerations which may completely invalidate such an optimization. For example, sheet and stringers may be preferred as components of a compression member; however, other design considerations such as discontinuities and attachment problems would preclude their use in a pressure vessel.

Figure 7.3 is a study of the use of materials for large-diameter (18 ft) tanks. When constant pressure lines are plotted, it is seen that most materials, with the possible exception of beryllium, are compression critical except at relatively high pressures. (The operating pressures of most liquid propellant systems are of the order of 20 to 70 lb/in.^{2})

It behooves the designer then, to improve the buckling efficiency of the vessel over that attainable with monocoque construction (figure 7.1). Since E/δ is almost a constant (except for beryllium), improvement in compressive efficiency must be accomplished by geometric design. One such technique is the use of a waffle-type construction, which has been used in the Thor and Saturn IV boosters for the reasons mentioned. Figure 7.4 illustrates the variation of the effectiveness of a waffle cylinder over that of a monocoque cylinder achieved by varying the waffle geometry. In the Saturn IV vehicle, selection of a waffle pattern for the tank section afforded a weight saving of approximately 30 percent over a monocoque structure, accounting for the compression and bending requirements. As a pressure vessel, approximately 85 percent of the waffle weight was

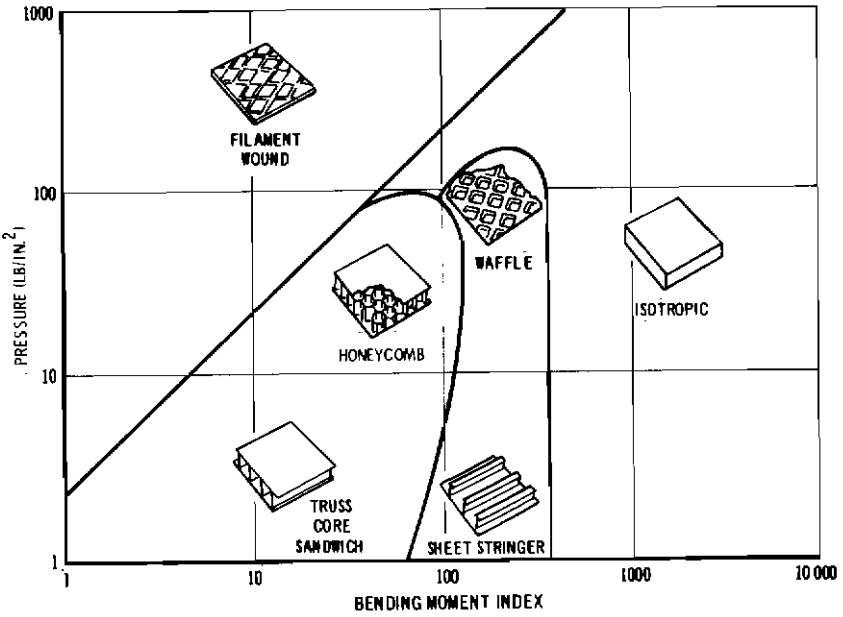

FIGURE 7.2—Minimum weight construction for cylinders under pressure and bending.

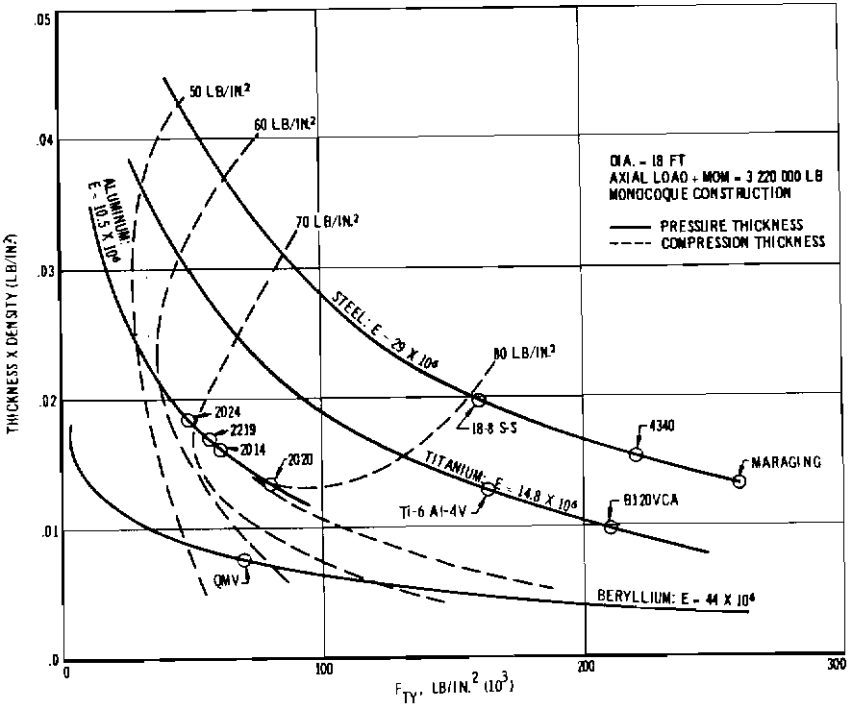

FIGURE 7.3—Pressure and compression thickness for 18-ft diameter vessel of various materiols.

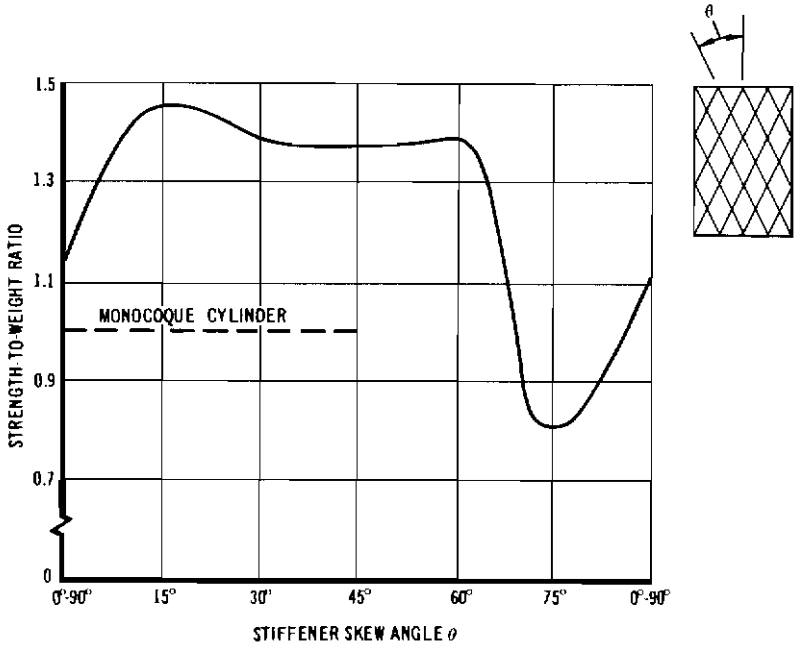

FIGURE 7.4—Typical variation of stiffener effectiveness with skew angle. Waffle-milled integrally stiffened cylinders.

effective in restraining pressure. This is also indicated in the example shown in figure 7.1.

There are three types of possible failure to be recognized in considering the buckling strength of an integrally stiffened cylinder: the general instability failure of the cylinder and two local buckling modes. One of these modes is a buckling of the skin between ribs of stiffeners as shown in figure 7.5. The other local failure involves the crippling or buckling of the stiffeners. Either of these local failures by itself does not necessarily mean a total collapse of the structure (see figure 7.5). However, when local buckling does occur, it reduces the theoretical overall buckling strength and, at worst, could cause a general instability failure.

The critical buckling stress for flat or curved plates is of the form

$$\sigma_{CR}=K\frac{\pi^2 E}{12(1-\mu^2)}\left(\frac{t_s}{\lambda_s}\right)^2$$

where

t_s=skin thickness
λ_s=rib spacing
μ=the Poisson ratio

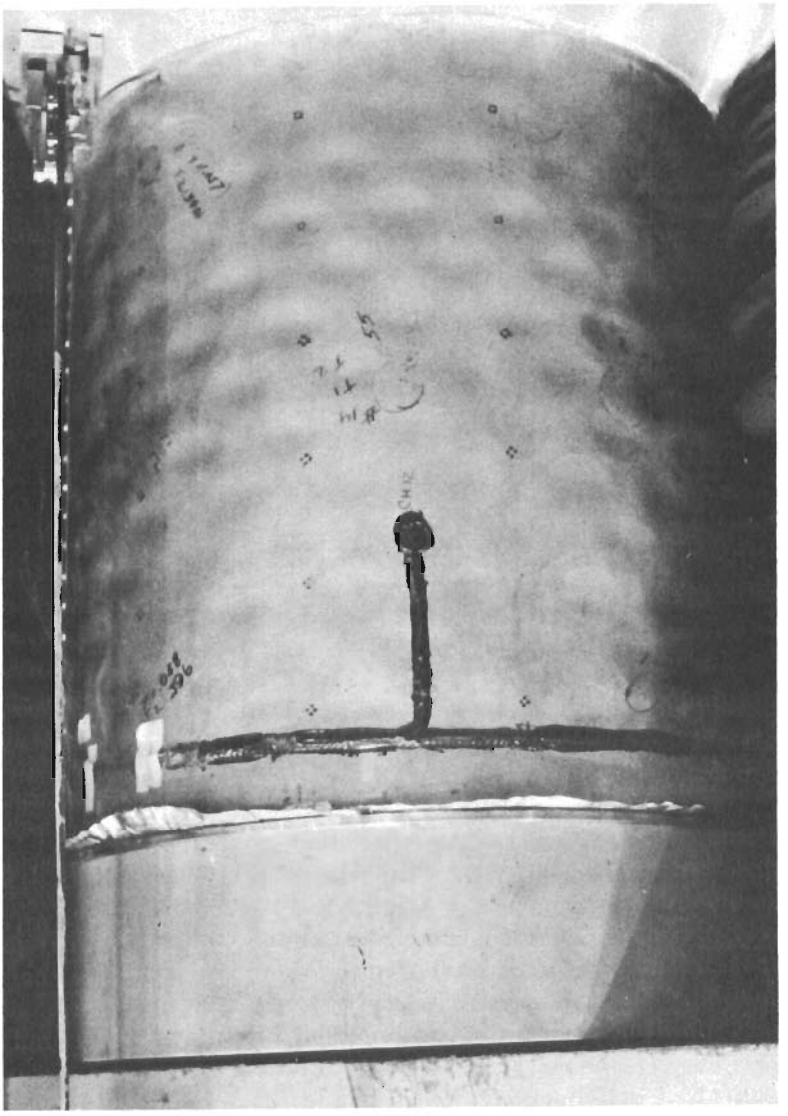

FIGURE 7.5—Instability failure of a cylinder due to buckling of the skin between ribs of stiffeners.

and K is a function of the dimension of the plate and the bending rigidity of the stiffeners.

Test results on skewed waffle patterns show that this equation reduces to the form

$$\sigma_{s_{CR}} = 7.0E\left(\frac{t_s}{\lambda_s}\right)^2$$

Similarly, the local crippling of the outstanding leg of the rib is expressed as

$$\sigma_{r_{CR}} = K_r E \left(\frac{t_{w_s}}{t_r}\right)^2$$

where

t_{w_s} = thickness of the outstanding leg

t_r = height of the outstanding leg

A satisfactory value of the buckling coefficient K_r has been found to be

$$K_r = 0.416$$

The stress in the skin and rib elements can be found by considering the portion of the total applied load carried by each element (fig. 7.6). This figure also illustrates how much of the stiffening material in a skewed waffle is effective in restraining pressure. This is why 85 percent efficiency in the use of stiffening material to restrain pressure was achieved in the Thor and Saturn designs. The total axial load can now be written as

$$P_x = P_s + P_r$$

or

$$\frac{N_x \lambda_s}{\cos\theta} = \frac{N_s \lambda_s}{\cos\theta} + 2 t_r t_{w_s} \sigma_r \cos\theta$$

$$= \frac{t_s \sigma_s \lambda_s}{\cos\theta} + 2 t_r t_{w_s} \sigma_r \cos\theta$$

All modes of failure have been treated separately up to this point, and the equations above provide an analytical technique. Hence, given certain geometrical dimensions and material properties, the critical buckling stress and load can be determined. While these equations are useful in stress analysis, they are very cumbersome for the structural designer. The use of equations in this form requires that the designer combine critical stress equations and geometric proportions

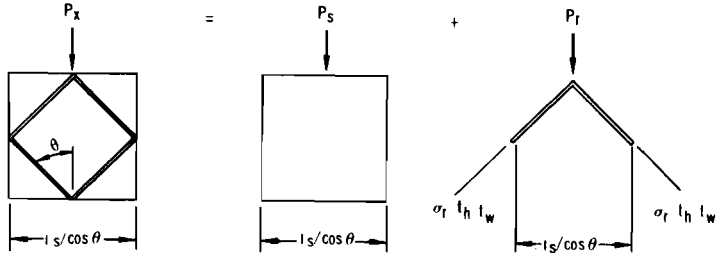

FIGURE 7.6—Stresses in skewed waffle.

and that he produce an optimum configuration by an iterative process. In order to reduce the geometric parameters, the designer must consider that the dimensional terms are normalized and working design charts such as shown in figure 7.7 can be created.

PRACTICAL CONSIDERATIONS

In many cases the optimum configurations represented by the envelope curve will prove to be impractical from a design or manufacturing viewpoint. For example, the optimum rib thickness may prove to be too thin or the optimum rib height too great. The rib height is particularly critical when the waffle sheet is to receive a subsequent forming operation such as rolling into a cylinder. Cost can also be a serious consideration. For the taller ribs, a greater quantity of the original plate stock will be discarded as chips. By limiting the rib thickness-height ratio a compromise between weight and practical limitations can be achieved. Figure 7.7 shows the deviation from optimum design dictated by manufacturing requirements.

The compromise made in this particular design will result in buckling stress on the rib which would make skin buckling the first failure mode. This is still a balanced design, since failure will still occur simul-

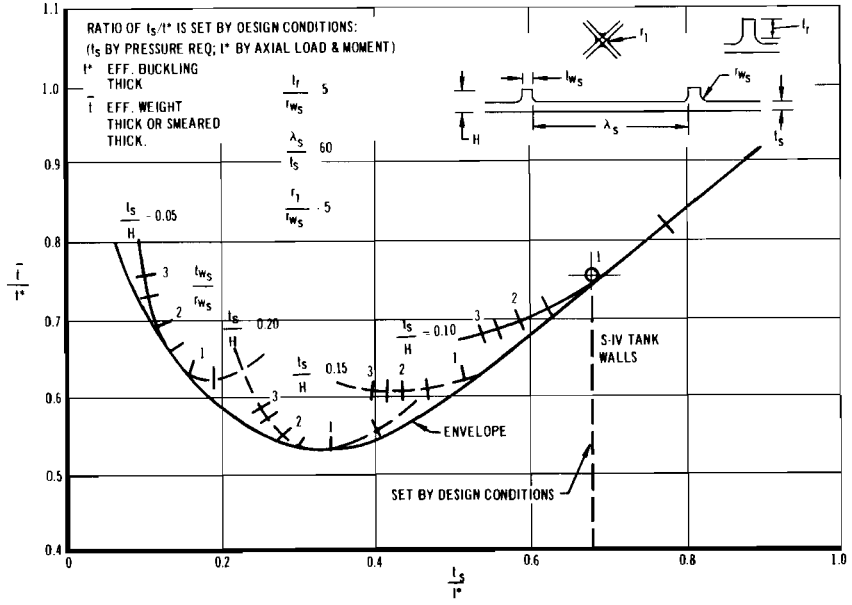

FIGURE 7.7—Design chart of 45° waffle-stiffened cylinders.

taneously in two of the three failure modes. The design may be considered nonoptimum, however, since all failure modes do not occur simultaneously.

Thus, what started out as a rather precise determination of optimum weight and geometry has now become involved with another parameter which is difficult to describe, namely, practical rib dimensions which are correlated with manufacturing techniques. Even such items as corner radii can produce a significant effect. Also, tolerances can have a significant weight influence in the manufacture of waffle-type structures.

Waffle structure may be manufactured by three techniques—chemical milling, machining, and forging—although forging is but little used. Chemical milling is a process whereby selective areas are exposed to chemical reagents which progressively remove the exposed metal. This process provides rather poor tolerance control, however; in fact, the tolerances of the chemical removal process must be added to the normal tolerances of the original materials. The undercutting of an outstanding leg is also a common fault, and the radii produced as the reagent erodes the material are rather generous. This process increases the nominal weight of the part because of the latitude of the tolerances involved.

On the other hand, the machining of the waffle structure from flat plate stock provides excellent tolerances which are consistent with normal machining operation. In addition, these tolerances are not additive to the original plate tolerances. Small values of r/s, and r/w consistent with good machine practice, are also achieved.

Thus, unless the part must be machined after forming to a complex contour, as in the case of a tank dome, machining of the waffle pattern is preferable to chemical milling.

INSTABILITY FAILURES

Even with the most efficient waffle or stiffened structure, however, there are loading conditions and other considerations which dictate the use of a sandwich structure (see figures 7.1 and 7.2). In the selection of a configuration for a sandwich structure, an attempt is made again to design for simultaneous local and general instability failure.

The local instability criteria of a truss-core sandwich, as described in reference 1, is

$$\sigma_{CR}=\frac{K\pi^2 E\eta}{12(1-\mu^2)}\left(\frac{t_f}{b_f}\right)^2$$

where

t_f=thickness of the sandwich face
b_f=pitch of the truss
η=plasticity reduction factor

An evaluation of the buckling coefficient K for a single and double core configuration is given in figures 7.8 and 7.9, respectively. These plots define two modes of instability: the buckling of the faces between the core, and the buckling of the core itself. For optimum design, the selection of the buckling coefficient is based on the simultaneous occurrence of these two failure modes (figure 7.10 shows the excellent agreement between test data and the theoretical method proposed by Anderson [1]). Then, an optimum configuration may be achieved by equating the general instability stress for the buckling of the cylinder to these local instability stresses.

The general instability of a truss-core sandwich cylinder for single corrugation may be expressed as

$$\sigma_{CR_S}=\frac{1.73CEt_fb_f \tan\theta}{R(2t_f+t_c/\cos\theta)}\sqrt{\frac{t_c}{6t_f\cos\theta}+1}$$

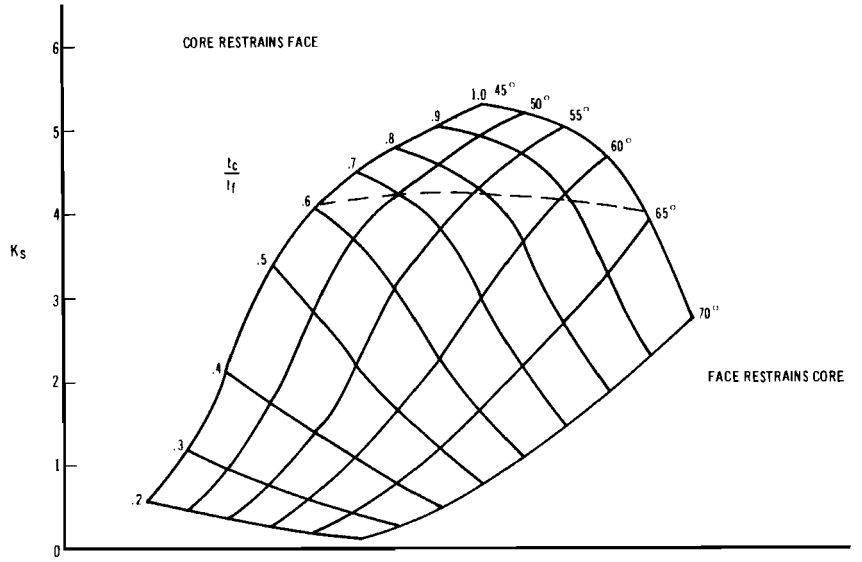

FIGURE 7.8—Local buckling coefficient for single truss-core sandwich plate.

[1] Anderson, Melvin S.: *Local Instability of the Elements of a Truss Core Sandwich Plate.* NASA TR R–30.

where

θ = the angle of the diagonal (see fig. 7.2)
t_c = thickness of the core

For a double corrugation configuration, this expression becomes

$$\sigma_{CR_S} = \frac{3.46CEt_f b_f \tan\theta}{R(2t_f + 2t_c/\cos\theta)} \sqrt{\frac{2t_c}{6t_f \cos\theta} + 1}$$

These instability stresses may then be equated to the local buckling stress.

The simplest method of predicting the parameters for an optimum design is by compression of the strength-weight ratio of the design so that this ratio is a maximum. The resulting ratio is also interpreted as being an efficiency index, which is expressed as

$$\frac{\text{strength}}{\text{weight}} = \text{efficiency index}$$

Here it is desirable to express strength as a function of load, geometry, and modulus of elasticity in nondimensional form,

$$\text{strength} = f\left(\frac{N}{ER}\right)$$

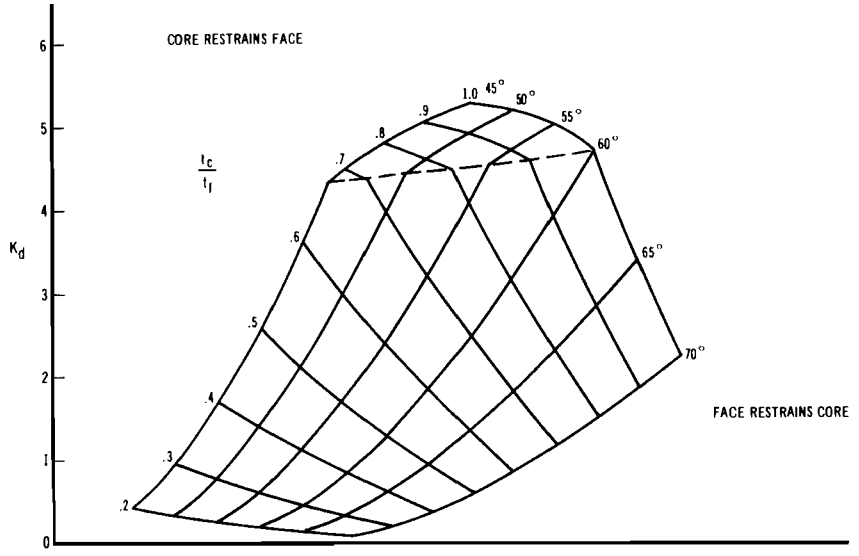

FIGURE 7.9—Local buckling coefficient for double truss-core sandwich plate.

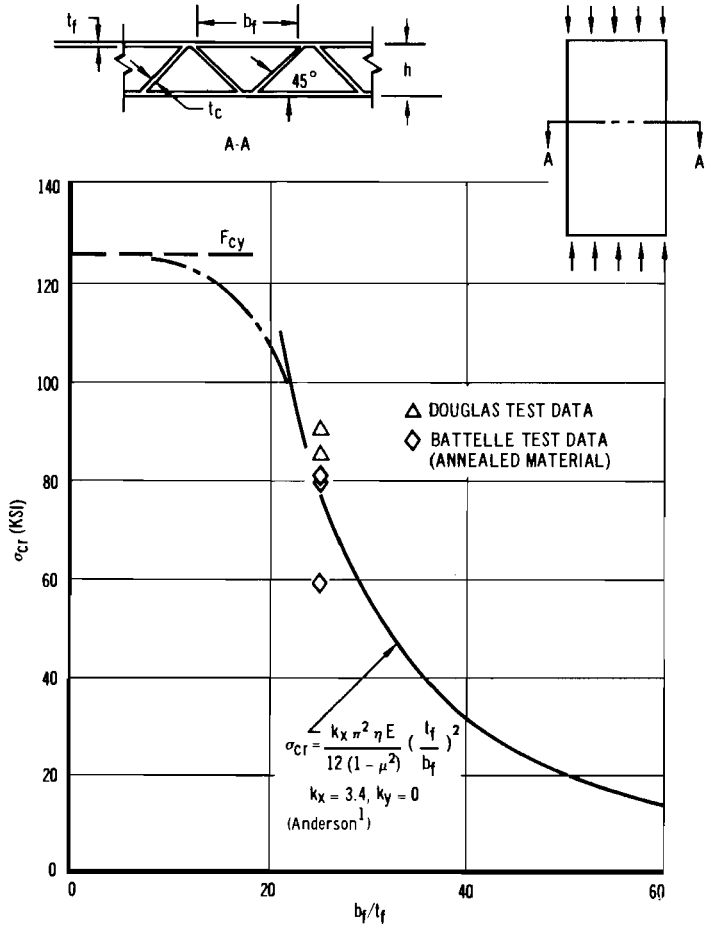

FIGURE 7.10—Titanium alloy (Ti–6Al–4V) roll-welded sandwich local instability compressure failure.

where

N=running load (lb/in.)

Since the efficiency is nondimensional, the weight parameter may be expressed nondimensionally by showing it to be a function of geometry and the "smeared thickness" (equivalent homogeneous plate thickness, $\bar{t}$),

$$\text{weight} = f = \left(\frac{\bar{t}}{R}\right)$$

In order to express the equations for local and general instability as functions of N/ER and $\bar{t}/R$ and to eliminate b_f from the stability

equations, we write

$$\sigma=\frac{N}{\bar{t}}=\frac{K_s K_d \pi^2 E}{12(1-\mu^2)}\left(\frac{t_f}{b_f}\right)^2$$

Solving for b_f

$$b_f=\pi t_f\left(\frac{K_s K_d E\bar{t}}{12(1-\mu^2)N}\right)^{1/2}$$

When the expression for local buckling stress is equated to that for general instability and the above relationship is substituted for b_f, the following expressions are derived for single corrugation

$$\frac{N}{ER}=\left(\frac{\bar{t}}{R}\right)^{5/3}\left\{C^{2/3}K_s^{1/3}\,1.395\left(\frac{t_c}{6t_f\cos\theta}+1\right)^{1/3}\left[\frac{\sin\theta\cos\theta}{\left(2\cos\theta+\frac{t_c}{t_f}\right)^2}\right]^{2/3}\right\}$$

and double corrugation

$$\frac{N}{ER}=\left(\frac{t}{R}\right)^{5/3}\left\{C^{2/3}K_d^{1/3}\,0.878\left(\frac{2t_c}{6t_f\cos\theta}+1\right)^{1/3}\left[\frac{\sin\theta\cos\theta}{\left(\cos\theta+\frac{t_c}{t_f}\right)^2}\right]^{2/3}\right\}$$

For simplicity, it is assumed that the cylinder buckling coefficient is of the classical value ($C=0.606$). The remaining efficiency terms are then maximized by substituting the proper values of K_s, K_d, and t_c/t_f given by Anderson.[2]

These results show that maximum efficiency is obtained when $\theta=55°$, $t_c/t_f=0.78$, and $K_s=4.23$ for the single corrugation; and $\theta=48°$, $t_c/t_f=0.70$, and $K_d=4.58$ for the double corrugation.

When these values are substituted in the above equations, the following relationships are attained for single and double corrugations, respectively.

$$\frac{N}{ER}=0.432\left(\frac{\bar{t}}{R}\right)^{5/3}$$

and

$$\frac{N}{ER}=0.467\left(\frac{\bar{t}}{R}\right)^{5/3}$$

These results indicate that the double corrugation is slightly more efficient than the single corrugation.

For purposes of simplification, the optimum design equations given above neglect the effect of core shear deformation and the variation of the buckling coefficient from the classical.

[2] *Ibid.*

FINAL OPTIMIZATION EQUATIONS

For the present, only the effects of the core shear stiffness will be discussed.

Since, in practice, the effect of core shear deflection is to reduce the effective buckling coefficient by a small amount, an approximate method of solution will be used.

Timoshenko and Gere [3] express the effect of shear deformation upon the buckling of homogeneous columns by the equation

$$P_{cr}=\frac{P_e}{1+\frac{nP_e}{AG}}$$

where

$$P_e=\frac{\pi^2 EI}{L^2}$$

n=shape factor
A=area
G=shear modulus
L=length

This equation may also be expressed as

$$N_{cr}=\frac{N_e}{1+\frac{N_e}{hG}}$$

where the shape factor is assumed to be 1, and hG is the transverse shear stiffness for homogeneous plates.

The transverse shear stiffness for a corrugated sandwich structure has two values, one in the direction of the corrugated core, and the other transverse to these corrugations. Since the shear stiffness transverse to these corrugations is much smaller than in the other direction, only the smallest need be considered here.

This transverse shear stiffness parameter has been evaluated for both single and double corrugation, assuming hinged joints, and is given by

$$U_s=\frac{t_c E \sin^2\theta \cos\theta}{(1-\mu^2)} \qquad \text{(single corrugation)}$$

and

$$U_d=\frac{2t_c E \sin^2\theta \cos\theta}{(1-\mu^2)} \qquad \text{(double corrugation)}$$

[3] Timoshenko, Stephen, and J. Gere: *Theory of Elastic Stability*. McGraw-Hill Book Co., Inc., 2nd ed., 1961.

Substituting these equations into the expression for shear stiffness gives

$$N_{cr_s}=\frac{N_{e_s}}{1+\frac{N_{e_s}(1-\mu^2)}{t_c E \sin^2\theta\cos\theta}} \qquad \text{(single corrugation)}$$

and

$$N_{cr_d}=\frac{N_{e_d}}{1+\frac{N_{e_d}(1-\mu^2)}{2t_c E \sin^2\theta\cos\theta}} \qquad \text{(double corrugation)}$$

For simplification, it is desirable to express N_e in the denominators in terms of the buckling coefficient C. For the buckling of a cylinder where $\sigma_{cr}=(CE_t{}^*)/R$ this may also be expressed as

$$N=\frac{CE_t{}^*\bar{t}}{R}$$

where t^* is the equivalent buckling thickness of the sandwich.

When the last three equations are combined and the final equation is expressed as a function of the buckling coefficient, the expression

$$C_{cr_s}=\frac{1}{\frac{1}{C_{e_s}}+\frac{t^*\bar{t}(1-\mu^2)}{Rt_c \sin^2\theta\cos\theta}}$$

is obtained for single corrugation, and

$$C_{cr_d}=\frac{1}{\frac{1}{C_{e_d}}+\frac{t^*\bar{t}(1-\mu^2)}{2Rt_c \sin^2\theta\cos\theta}}$$

is obtained for double corrugation. These equations then reflect the change in the buckling coefficient due to the shear stiffness of the core.

This analysis is based upon a semi-empirical theory that is dependent upon the experimental results of monocoque cylinders. Since the buckling coefficient is a function of the thickness to radius ratio of monocoque cylinders, this theory contends that this ratio is also applicable to sandwich cylinders. For sandwich construction, this thickness can be shown to be a function of the equivalent "buckling thickness" t^*.

The empirical monocoque curve used here bases the dependency of the buckling coefficient to the thickness-to-radius ratio on results

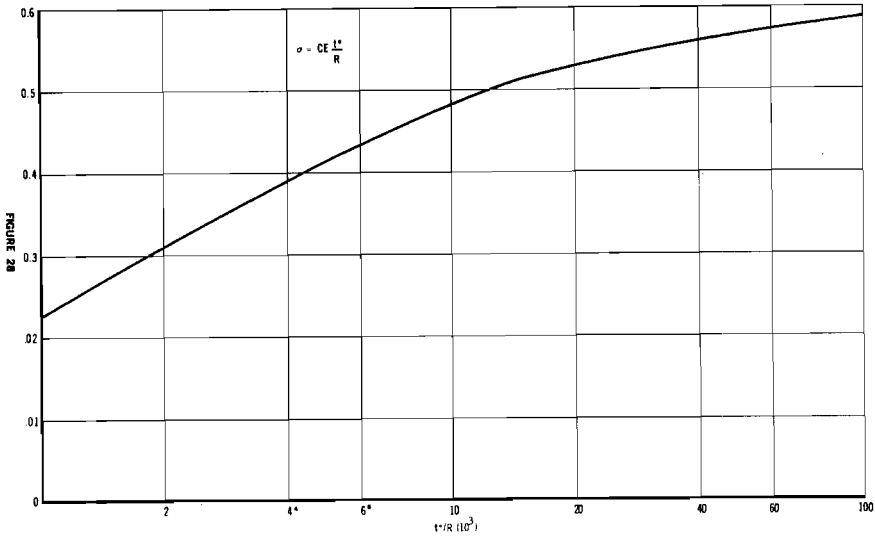

FIGURE 7.11—Classical coefficient C=0.606.

given by Gerard and Becker.[4] An average imperfection parameter U equal to 0.00015 will be used. This curve is plotted in figure 7.11.

For purposes of evaluating the variation in the buckling coefficient, it is required that the empirical curve from figure 7.11 be expressed analytically. By inspection, a hyperbolic function of the form $y=[x/(a+bx)]+c$ seems to describe the curve adequately.

When the constants of the above equation are determined by a method of averages, the following equation is obtained:

$$C_e=\frac{\frac{t^*}{R}-1\times10^{-3}}{7.52\times10^{-3}+2.76\,\frac{t^*}{R}}+0.23$$

Simplifying the above equation gives

$$C_e=0.097\left(\frac{2.24\times10^3\,\frac{t^*}{R}+1}{0.367\times10^3\,\frac{t^*}{R}+1}\right)$$

[4] Gerard, George, and Becker, Herbert: *Handbook of Structural Stability.* Part III. NASA TN-D163, Sept. 1959.

Substituting this equation into the previous results gives

$$C_{cr_s}=\frac{1}{\dfrac{0.367\times10^3\dfrac{t^*}{R}+1}{0.097\left(2.24\times10^3\dfrac{t^*}{R}+1\right)}+\dfrac{t^*\bar{t}(1-\mu^2)}{Rt_c\sin^2\theta\cos\theta}}$$

and

$$C_{cr_d}=\frac{1}{\dfrac{0.367\times10^3\dfrac{t^*}{R}+1}{0.097\left(2.24\times10^3\dfrac{t^*}{R}+1\right)}+\dfrac{t^*\bar{t}(1-\mu^2)}{2Rt_c\sin^2\theta\cos\theta}}$$

The aim, of course, is to substitute the above equations for C_{cr_s} and C_{cr_d} into the original buckling equations. It is desirable, for purposes of optimization, to express these equations in similar terms, that is, to evaluate t^* in terms of the other parameters expressed in the original buckling equations. We write

$$t_s^*=\frac{1.73t_fb_f\tan\theta}{2t_f+\dfrac{t_c}{\cos\theta}}\sqrt{\frac{t_c}{6t_f\cos\theta}+1}$$

and

$$t_d^*=\frac{1.73t_fb_f\tan\theta}{t_f+\dfrac{t_c}{\cos\theta}}\sqrt{\frac{2t_c}{6t_f\cos\theta}+1}$$

Solving the equated buckling and instability equations on page 51 for b_f and substituting into the equations for t^* and solving for t^*/R gives for single corrugation

$$\frac{t^*}{R}=\frac{(1.73\pi)^{2/3}}{\{12(1-\mu^2)\tan\theta\}^{1/3}}\left(\frac{K_x}{C_{e_s}}\right)^{1/3}\left(\frac{\bar{t}}{R}\right)^{2/3}\frac{1}{\left(2+\left(\dfrac{t_c}{t_f\cos\theta}\right)\left(\dfrac{t_c}{6t_f}+1\right)\right)}$$

and for double corrugation

$$\frac{t^*}{R}=\frac{(1.73\pi)^{2/3}}{\{12(1-\mu^2)\tan\theta\}^{1/3}}\left(\frac{K_x}{C_{e_d}}\right)^{1/3}\left(\frac{\bar{t}}{R}\right)^{2/3}\frac{1}{\left(1+\left(\dfrac{t_c}{t_f\cos\theta}\right)\left(\dfrac{2t_c}{6t_f}+1\right)\right)}$$

For simplification, the buckling coefficient C_e in the above equations will be approximated by assuming the value to be 0.606 (the classical

coefficient). A small error is necessarily introduced by this simplification, but in the region of practical interest this error is negligible.

If we let

$$\alpha=2\cos\theta+\frac{t_c}{t_f}$$

$$\beta=\frac{t_c}{6t_f\cos\theta}+1$$

$$\mu=0.30$$

solving for C_{cr_s}, we obtain the expression

$$C_{cr_s}=\frac{1}{\dfrac{\dfrac{(01K_s^{1/3}\cos\theta}{(\tan\theta)^{1/3}\alpha\beta}\left(\dfrac{\bar{t}}{R}\right)^{2/3}+1}{0.097\left(\dfrac{3670K_s^{1/3}\cos\theta}{(\tan\theta)^{1/3}\alpha\beta}\left(\dfrac{\bar{t}}{R}\right)^{2/3}+1\right)}+\dfrac{1.63}{\beta\sin^2\theta\cos\theta}\left(\dfrac{\bar{t}}{R}\right)^{2/3}\left(\dfrac{K_s}{\tan\theta}\right)^{1/3}\dfrac{t_f}{t_c}}$$

for single corrugation.

Similarly, if

$$\gamma=\cos\theta+\frac{t_c}{t_f}$$

$$\lambda=\frac{2t_c}{6t_f\cos\theta}+1$$

$$\mu=0.30$$

solving for C_{cr_d}, we obtain

$$C_{cr_d}=\frac{1}{\dfrac{\dfrac{475K_d^{1/3}\cos\theta}{(\tan\theta)^{1/3}\gamma\lambda}\left(\dfrac{\bar{t}}{R}\right)^{2/3}+1}{0.097\left[\dfrac{2900K_d^{1/3}\cos\theta}{(\tan\theta)^{1/3}\gamma\lambda}\left(\dfrac{\bar{t}}{R}\right)^{2/3}+1\right]}+\dfrac{1.29}{\lambda\sin^2\theta\cos\theta}\left(\dfrac{\bar{t}}{R}\right)^{2/3}\left(\dfrac{K_d}{\tan\theta}\right)^{1/3}\dfrac{t_f}{t_c}}$$

for double corrugation. Therefore, by substituting C_{cr_s} and C_{cr_d} for C, and simplifying, we obtain

$$\frac{N}{ER}=\left(\frac{\bar{t}}{R}\right)^{5/3}\left\{C_{cr_s}{}^{2/3}K_s^{1/3}1.395\beta^{1/3}\left(\frac{\sin\theta\cos\theta}{\alpha^2}\right)^{2/3}\right\}$$

and

$$\frac{N}{ER}=\left(\frac{\bar{t}}{\bar{R}}\right)^{5/3}\left\{C_{cr_d}{}^{2/3}K_d{}^{1/3}0.878\lambda^{1/3}\left(\frac{\sin\theta\cos\theta}{\gamma^2}\right)^{2/3}\right\}$$

The efficiency index is described as the terms inside the large bracket. Maximizing the efficiency index results in two solutions for the core geometry for these equations.

These equations are evaluated and plotted in figure 7.12 for those core geometries showing maximum efficiency. Because of the negligible differences in the computed efficiency between $\theta=50°$ and $55°$ for the single corrugation, and between $\theta=48°$ and $50°$ for the double corrugation, we may arbitrarily select $\theta=50°$ in both cases for the purpose of simplification and practical application. The maximum efficiency for the single and double corrugation is then

$$\theta=50°;\ \frac{t_c}{t_f}=0.69;\ K_s=4.20$$

and

$$\theta=50°;\ \frac{t_c}{t_f}=0.74;\ K_d=4.40$$

respectively.

To eliminate the necessity of evaluating the buckling coefficient C_{cr_s} and C_{cr_d} each time a solution is required, we may express the

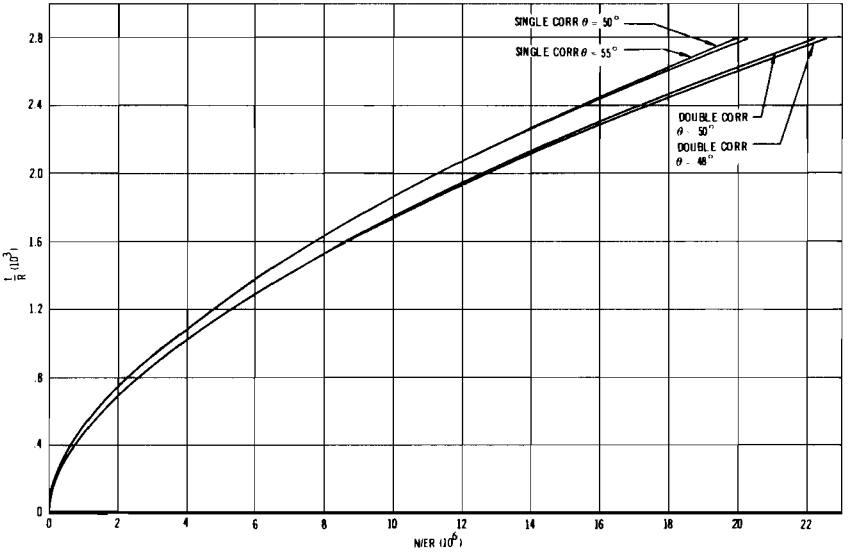

FIGURE 7.12—Core geometry for both single and double corrugation showing maximum efficiency.

curves shown in figure 7.12 analytically. Since a parabolic curve of the form $y=ax^b$ accurately describes the curve, the resulting equations may be expressed as

$$\frac{N}{ER}=0.606\left[\frac{\bar{t}}{R}\right]^{1.75}$$

for single corrugation, and

$$\frac{N}{ER}=0.601\left(\frac{\bar{t}}{R}\right)^{1.74}$$

for double corrugation.

In sandwich design the allowable buckling stress frequently exceeds the elastic limit of the material. In this case an iterative procedure is necessary to evaluate correctly the tangent modulus of elasticity at the final condition of stress using the above equations.

This iterative procedure may be circumvented if the latter equations are expressed in terms of the loading index and the material property. By substituting the relation $N/\sigma=\bar{t}$ and by associating the tangent modulus strain by the symbol A, where $A=\sigma/E_t$, the expression

$$A\sigma^{0.75}=0.606\left(\frac{N}{R}\right)^{0.75}$$

is obtained for single corrugation, and

$$A\sigma^{0.75}=0.601\left(\frac{N}{R}\right)^{0.74}$$

for double corrugation with the aid of geometrical relationships shown below.

Single Corrugation	*Double Corrugation*
$t_f=\frac{\bar{t}}{3.07}$	$t_f=\frac{\bar{t}}{4.31}$
$t_c=0.69t_f$	$t_c=0.74t_f$
$T=\frac{1.16t_f}{\sqrt{A}}$	$T=\frac{2.37t_f}{\sqrt{A}}$

Using these equations and geometrical relationships, the development of the nomogram shown in figures 7.13 and 7.14 is possible. The critical buckling stress (σ) and the face and core thickness (t_f, t_c)

for an aluminum alloy (7075–T6) and a titanium alloy (Ti-6Al-4V) are shown in the nomogram. The tangent modulus of elasticity for the aluminum and titanium alloys are shown in figures 7.15 and 7.16, respectively. To effect a solution for other materials, it is only necessary to compute the parameter $A\sigma^{0.75}$ and/or $A\sigma^{0.74}$ for the particular material in question, and plot the results in the existing nomogram.

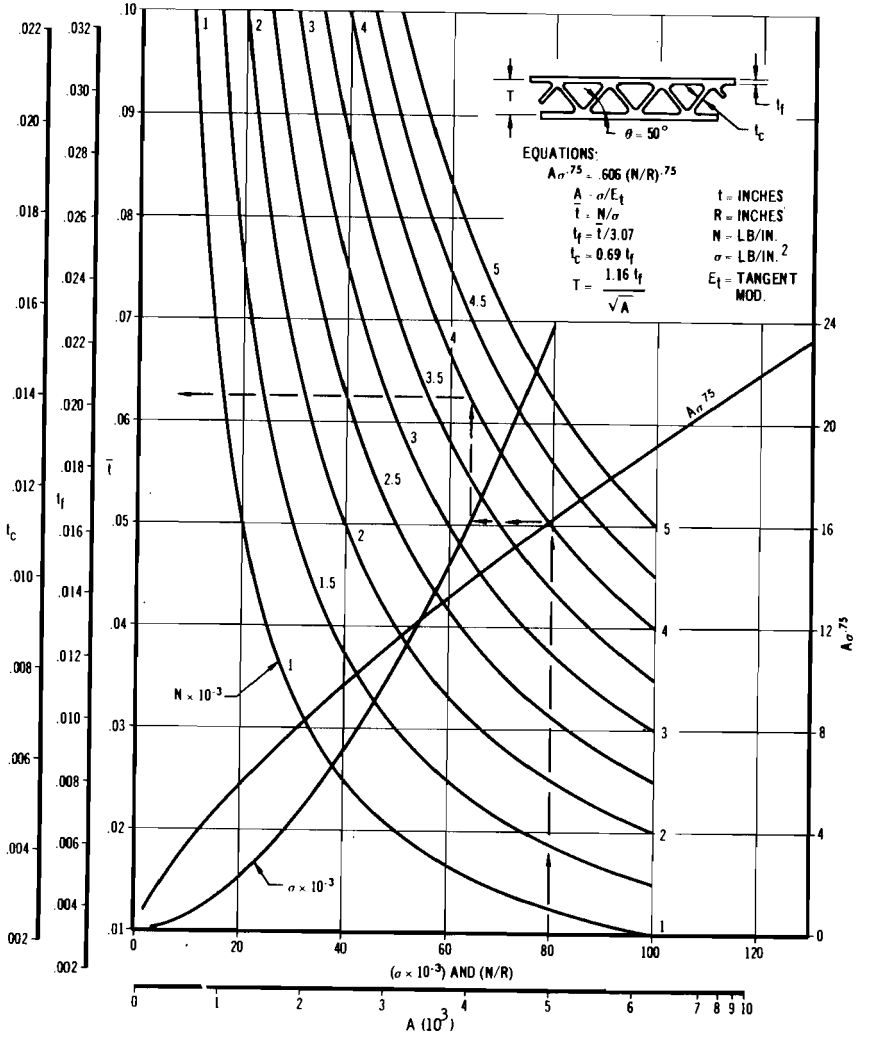

FIGURE 7.13—Optimum design of truss-core sandwich cylinders with single corrugation.

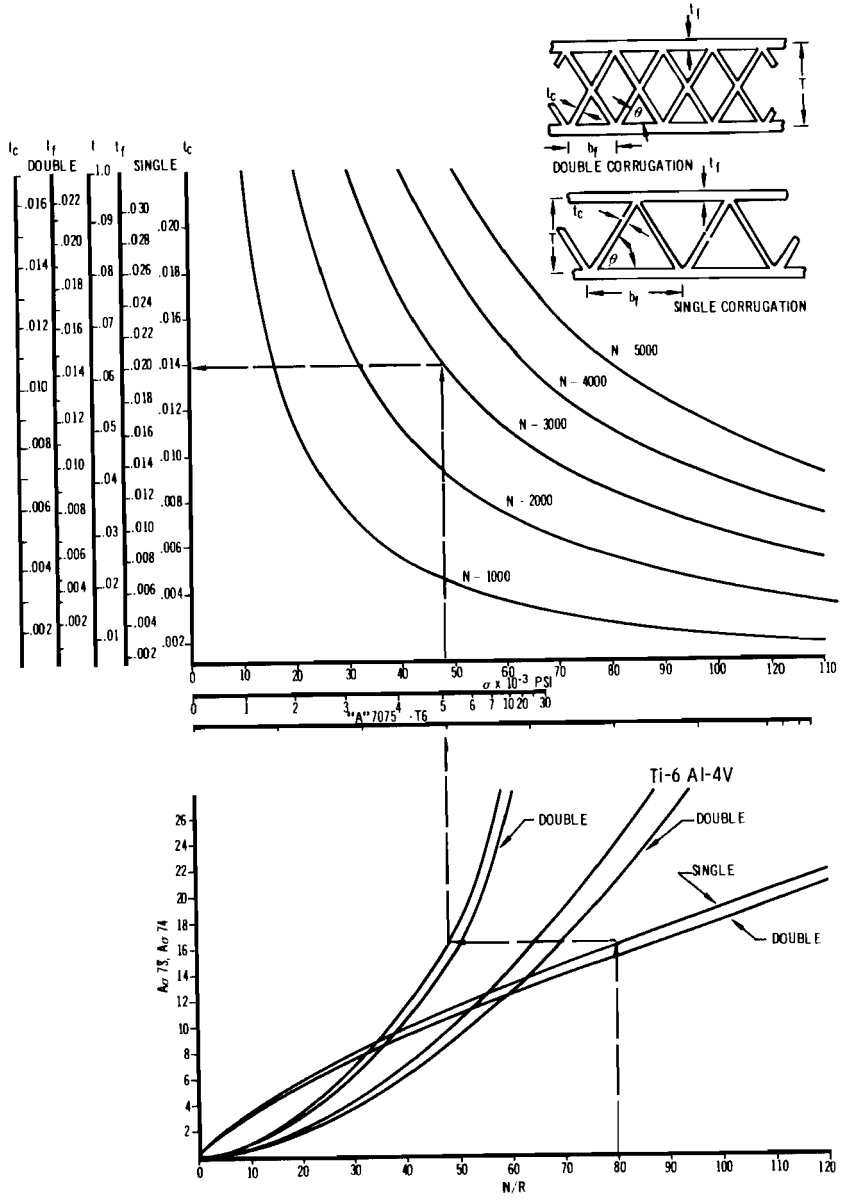

FIGURE 7.14—Optimum design of truss-core sandwich cylinders under axial compression.

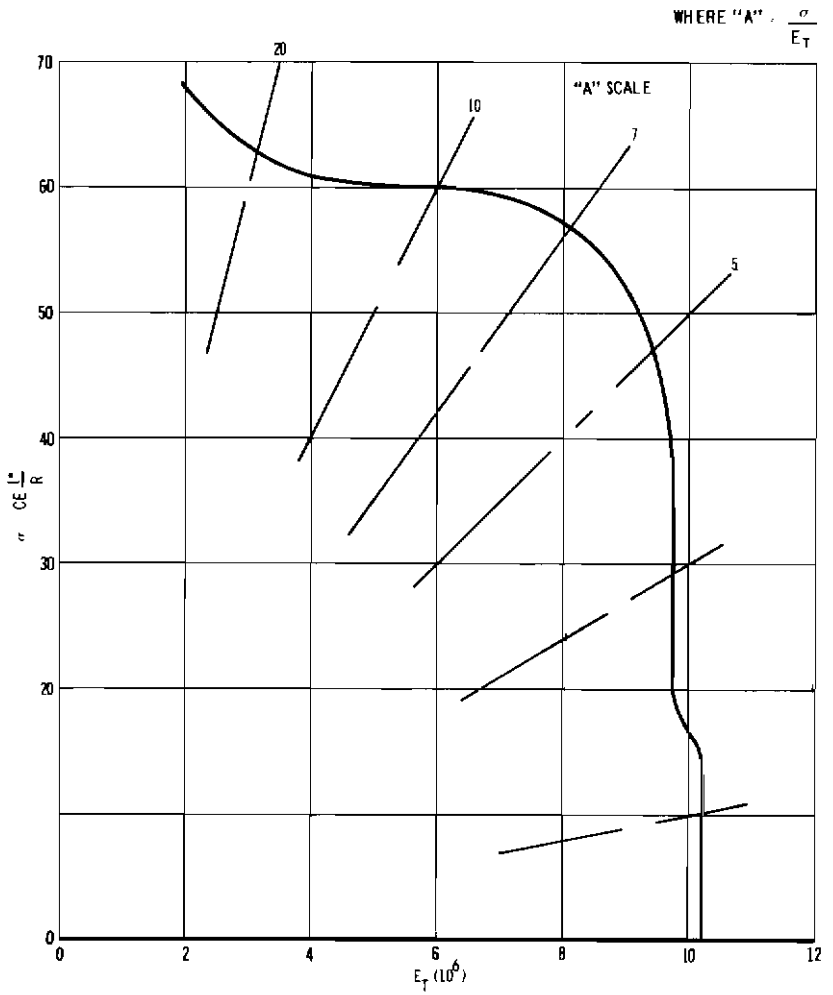

FIGURE 7.15—Tangent modulus of elasticity for aluminum alloy.[4] [Sacks, G., and R. Ford Pray III, eds.: Air Weapons Materials Application Handbook—Metals and Alloys. Air Research and Development Command, ARDC–TR–59–66.]

[4] *Ibid.*

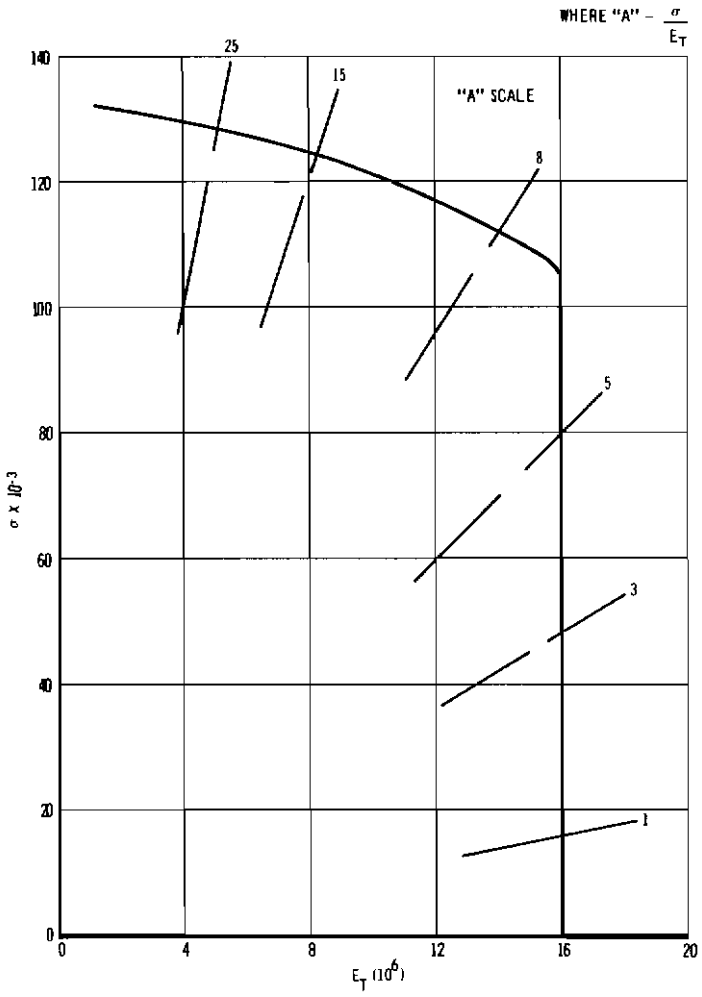

FIGURE 7.16—Tangent modulus of elasticity for titanium alloy.[4] Annealed Ti-6Al-4V alloy. Typical value—compression at R.T. [Sacks, G., and R. Ford Pray III, eds.: Air Weapons Materials Application Handbook—Metals and Alloys. Air Research and Development Command, ARDC–TR–59–66.]

[4] *Ibid.*

EXAMPLE

Given: $N=3\ 000$ lb/in.
$R=37.5$ inches
Material: clad 7075–T6 aluminum alloy at room temperature

Find: The allowable buckling stress and geometry for single truss-core sandwich for optimum design

SOLUTION

Single corrugation

$$\frac{N}{R}=\frac{3\ 000}{37.5}=80$$

FROM NOMOGRAM FIGURE 7.13

$\sigma_f=48000$ lb/in.^{2}
$A=5.1\times10^{-3}$
$t_c=0.014$ in.
$t_f=0.020$ in.
$t=0.062$ in.
$T=\dfrac{1.16t_f}{\sqrt{A}}=0.325$ in.

CHAPTER 8

The Common Bulkhead

IN ORDER TO SHORTEN the interstage structure between tanks it has become increasingly important to provide a common bulkhead or dome between the two vessels. With hypergolic fluids, a twin nesting pair of bulkheads is necessary to avoid catastrophe in the event of a leak. A dual wall will provide a degree of insulation for cryogenic fluids. A double-wall common bulkhead designed of sandwich material provides a safe, insulative structure. Since such domes are generally formed hy pressure which tends to buckle the dome in compression the sandwich material will also provide an efficient structure.

The analysis presented here will be concerned primarily with establishing the general buckling stability criteria due to an external pressure force. Local instability failures such as wrinkling or dimpling will not be considered.

The huckling stability of sandwich spherical caps will be related to the buckling of monocoque spherical caps by "equivalency," which is a method of determining the required configuration of sandwich construction which has the same buckling stress as a monocoque spherical cap.

The buckling of monocoque spherical caps can be shown to be a function of the nondimensional geometric parameter λ and the nondimensional buckling parameter P which are defined as

$$\lambda=[12(1-\mu^2)]^{1/4}\frac{a}{\sqrt{Rh}} \tag{8.1}$$

$$P=\frac{1-\mu^2}{E}\left(\frac{a}{h}\right)^4 q_{cr} \tag{8.2}$$

where:

R = spherical radius, in.
h = thickness of shell, in.
E = modulus of elasticity, lb/in.^{2}
a = base radius of shell, in.
μ = the Poisson ratio

The basic equations defining the buckling stability of spherical caps as given in equations (8.1) and (8.2) may be related to sandwich shells once the equivalent buckling relationships are established.

To establish the equivalence of λ in equation (8.1) to that of a sandwich shell, it is necessary to derive the expression for λ. Timoshenko and Gere [1] have shown that the critical buckling strength of a monocoque cylinder under axial compression may be expressed as

$$\sigma_{cr}=\frac{N_{cr}}{h}=D\left[\frac{m^2\pi^2}{hL^2}+\frac{EL^2}{R^2Dm^2\pi^2}\right] \tag{8.3}$$

where

D=the bending rigidity$=Eh^3/[12(1-\mu^2)]$
R=the radius of cylinder
m=number of half-waves
L=length of cylinder

The general buckling equation of plates and shells may also be expressed as

$$\sigma_{cr}=\frac{K\pi^2D}{L^2h} \tag{8.4}$$

where K is the nondimensional buckling coefficient dependent upon the shell and plate geometry.

Equating equations (8.3) and (8.4) and solving for K gives

$$K=m^2+\frac{EL^4h}{R^2Dm^2\pi^4} \tag{8.5}$$

The buckling of cylinders under axial compressive forces and the buckling of spherical caps under external pressure have been shown by previous investigators as having the same expressions when the base radius (a) is substituted for the length (L) in the stability equation. Therefore, by substituting a for L in equation (8.5) we obtain

$$K=m^2+\frac{Ea^4h}{R^2Dm^2\pi^4} \tag{8.6}$$

Substituting $D=EI/(1-\mu^2)$ into equation (8.6) yields

$$K=m^2+\frac{a^4h(1-\mu^2)}{R^2Im^2\pi^4} \tag{8.7}$$

---

[1] Timoshenko, Stephen, and Gere, J.: *Theory of Elastic Stability.* McGraw-Hill Book Co., Inc., 2nd ed., 1961.

Since the number of half-waves may be assumed to be the same for both monocoque and sandwich cylinders, it is apparent that only the term

$$\frac{a^4h(1-\mu^2)}{R^2I}$$

need be evaluated to establish an equivalency. Setting this term equal to λ^4 gives

$$\lambda^4=\frac{a^4h(1-\mu^2)}{R^2I} \tag{8.8}$$

Since $h/I=1/\rho^2$ for a condition of unit width, substituting this into equation (8.8) gives

$$\lambda^4=\frac{(1-\mu^2)a^4}{R^2\rho^2} \tag{8.9}$$

or

$$\lambda=(1-\mu^2)^{1/4}\frac{a}{\sqrt{R\rho}} \tag{8.10}$$

Since $\rho=\frac{h}{\sqrt{12}}$ for homogeneous plates,

$$\lambda=[12(1-\mu^2)]^{1/4}\frac{a}{\sqrt{Rh}} \tag{8.11}$$

Equation (8.11), describing λ, is the same as equation (8.1).

It has been shown that the relationship between the buckling of a monocoque cylinder and a sandwich cylinder are a direct function of the radius of gyration ρ; therefore, to express λ in terms of a sandwich spherical cap, it is only necessary to substitute the sandwich radius of gyration in equation (8.10).

Assuming the face thicknesses are equal and isotropic, have the same modulus of elasticity, and the faces take the membrane stresses, the radius of gyration is

$$\rho=\frac{t_c+t_f}{2}$$

(where the moment of inerta of the individual faces is neglected). Substituting this value into equation (8.10) gives

$$\lambda_s=[4(1-\mu^2)]^{1/4}\frac{a}{\sqrt{R(t_c+t_f)}} \tag{8.12}$$

Equating equation (8.11) and equation (8.12) and solving for h gives

$$h=1.73(t_c+t_f) \tag{8.13}$$

The relationship between monocoque and sandwich structure from equation (8.13) was set equivalent to t^*, or

$$t^*=h=1.73(t_c+t_f)$$

Substituting $t^*=h$ in equation (8.11) gives

$$\lambda=[12(1-\mu^2)]^{1/4}\frac{a}{\sqrt{Rt^*}} \tag{8.14}$$

Equation (8.12) and equation (8.14), defining λ, are equal for the conditions assumed.

To account for face materials and face thicknesses which are not equal (neglecting the bending stiffness of the individual faces) the more general derivation of the equivalent buckling thickness t^* is expressed as

$$t^*=\frac{1.73}{E_{1_s}t_1+E_{2_s}t_2}\sqrt{(E_{1_s}t_1+E_{2_s}t_2)E_{1_s}t_1\left[(2t-t_1)^2\frac{E_{2_s}t_2^3}{E_{1_s}t_1}\right]-[E_{1_s}t_1(2t-t_1)+E_{2_s}t_2^2]^2} \tag{8.15}$$

To evaluate the nondimensional buckling parameter P in equation (8.2) to an equivalent sandwich spherical cap, the similarity of the classical buckling equations for cylinders under axial compression and spherical caps under external pressure will be applied.

According to Timoshenko and Gere,[2] the buckling of monocoque spherical caps and cylinders may be expressed as

$$\sigma_{cr}=CE\frac{h}{R} \tag{8.16}$$

or, in terms of the buckling pressure, as

$$\sigma_{cr}=\frac{qR}{2h} \tag{8.17}$$

Equating equations (8.16) and (8.17) and solving for q_{cr} gives

$$q_{cr}=2CE\left(\frac{h}{R}\right)^2 \tag{8.18}$$

Substituting equation (8.18) into equation (8.2) for q gives

$$P=\frac{2(1-\mu^2)a^4C}{h^2R^2} \tag{8.19}$$

[2] *Ibid.*

The term $[a^4(1-\mu^2)]/h^2R^2$ in equation (8.19) may be expressed also in terms of λ by a modification of equation (8.8) as

$$\frac{a^4(1-\mu^2)}{h^2R^2}=\frac{\lambda^4}{12}$$

and substituting in equation (8.19) yields

$$P=\frac{\lambda^4 C}{6} \tag{8.20}$$

Since λ has already been evaluated for sandwich construction from equation (8.14) it is only necessary to evaluate the nondimensional parameter C in equation (8.20) for sandwich construction.

The critical buckling stress for sandwich cylinders has been shown to be

$$\sigma_{cr}=\frac{CE_t t^*}{R} \tag{8.21}$$

or, in terms of the buckling pressure, for sandwich faces of equal thickness and modulus of elasticity

$$\sigma_{cr}=\frac{qR}{4t_f} \tag{8.22}$$

Equating equation (8.21) and equation (8.22) and solving for C gives

$$C=\frac{qR^2}{4E_t t^* t_f} \tag{8.23}$$

Substituting C from equation (8.23) and λ from equation (8.14) into equation (8.20) results in

$$P=\frac{(1-\mu^2)a^4 q_{cr}}{2E_t t^{*3} t_f} \tag{8.24}$$

Equation (8.24) is the equivalent expression for sandwich construction when the face thicknesses are equal and the face moduli of elasticity are the same.

Equation (8.24) expressed in terms of the buckling stress results in

$$P=\frac{2(1-\mu^2)a^4\sigma_{cr}}{E_t t^{*3} R} \tag{8.25}$$

To express equations (8.24) and (8.25) for sandwich structure of different face moduli and unequal face thickness where $E_1 \neq E_2$ and $t_1 \neq t_2$, it is only necessary to equate the buckling strains and satisfy the condition of equilibrium.

Equating $\epsilon_1=\epsilon_2$, where

$$\epsilon_1=\frac{\sigma_1}{E_{1_t}};\ \epsilon_2=\frac{\sigma_2}{E_{2_t}}$$

gives

$$\sigma_2=\frac{\sigma_1 E_{2_t}}{E_{1_t}} \tag{8.26}$$

From the condition of equilibrium $N_1+N_2=N$ where

$$N_1=\sigma_1 t_1;\ N_2=\sigma_2 t_2$$

gives

$$\sigma_1 t_1+\sigma_2 t_2=N \tag{8.27}$$

Substituting equation (8.26) into equation (8.27) and solving, result in:

$$\sigma_2=\frac{E_{2_t}N}{(E_{1_t}t_1+E_{2_t}t_2)}$$

and

$$\sigma_1=\frac{E_{1_t}N}{(E_{1_t}t_1+E_{2_t}t_2)}$$

Since $N=q_{cr}R/2$, substituting this value in the above equations gives:

$$\frac{\sigma_2}{E_{2_t}}=\frac{q_{cr}R}{2(E_{1_t}t_1+E_{2_t}t_2)}$$

and

$$\frac{\sigma_1}{E_{1_t}}=\frac{q_{cr}R}{2(E_{1_t}t_1+E_{2_t}t_2)}$$

Substitution into equation (8.25) results in

$$P=\frac{(1-\mu^2)a^4 q_{cr}}{t^{*3}(E_{1_t}t_1+E_{2_t}t_2)} \tag{8.28}$$

Or equation (8.28) in terms of σ_1, σ_2 gives

$$P=\frac{2(1-\mu^2)a^4\sigma_1,\ \sigma_2}{t^{*3}RE_{1_t},\ E_{2_t}} \tag{8.29}$$

The buckling equations (8.28) and (8.29) do not consider the effect of shear deformation of the core. In practice, the shear deformation is of significance because of the lack of shear rigidity of the core. To account for this shear deflection, use is made of the discussion by

Timoshenko and Gere [3] of the effect of the shearing deformation in the buckling of solid isotropic columns by the equation

$$F_{cr}=\frac{Fe}{1+\frac{nFe}{AG}} \tag{8.30}$$

where

$Fe=\frac{\pi^2 EI}{L^2}$

n=shape factor
A=area
G=shear modulus

Equation (8.30) may also be expressed as

$$N_{cr}=\frac{Ne}{1+\frac{Ne}{tG}} \tag{8.31}$$

where the shape factor is assumed to be 1, and the width 1.

Since the buckling of a spherical cap and a column are related, equation (8.31) will be used to express the effect of the shearing deformation upon the buckling of a sandwich spherical cap. From equation (8.28) where

$$P=\frac{(1-\mu^2)a^4 q_{cr}}{t^{*3}(E_{1_t}t_1+E_{2_t}t_2)}$$

the parameter q_{cr} will be expressed in terms of Ne by substituting $q_{cr}=2Ne/R$ and solving for N. Therefore,

$$Ne=\frac{Pt^{*3}R(E_{1_t}t_1+E_{2_t}t_2)}{2(1-\mu^2)a^4} \tag{8.32}$$

Letting the denominator $1+Ne/tG$ in equation (8.31) be equal to η, equation (8.31) may be written as

$$N_{cr}=\frac{Ne}{\eta}$$

The shear stiffness parameter for sandwich construction equivalent to the value of (tG) in equation (8.31) is

$$\frac{t(t+t_c)G_c}{2t_c} \tag{8.33}$$

[3] *Ibid.*

where the shear stiffness of the face is neglected. Substituting this equivalent sandwich value of shear stiffness and Ne from equation (8.32) and (8.33) and solving for η gives

$$\eta=1+\frac{Pt^{*3}Rt_c(E_{1_t}t_1+E_{2_t}t_2)}{(1-\mu^2)a^4tG_c(t+t_c)} \tag{8.34}$$

Since the faces may be considered thin with respect to the core thickness in most cases of sandwich design, it may be assumed that

$$tc\approx t$$

Therefore, equation (8.34) reduces to

$$\eta=1+\frac{Pt^{*3}R(E_{1_t}t_1+E_{2_t}t_2)}{2(1-\mu^2)a^4tG_c} \tag{8.35}$$

From equation (8.14) where $\lambda=[12(1-\mu^2)]^{1/4}\ a/\sqrt{Rt^*}$, this may also be expressed as

$$\frac{Rt^{*2}}{a^4(1-\mu^2)}=\frac{12}{\lambda^4R} \tag{8.36}$$

Substituting into equation (8.35) gives

$$\eta=1+\frac{6Pt^*(E_{1_t}t_1+E_{2_t}t_2)}{\lambda^4RtG_c} \tag{8.37}$$

From equation (8.13) where $t^*=1.73(t_c+t_f)$ assume that $t_c+t_f\approx t$ Using this simplifying assumption, equation (8.37) reduces to

$$\eta=1+\frac{12\times1.73P(E_{1_t}t_1+E_{2_t}t_2)}{\lambda^42G_cR} \tag{8.38}$$

Since $N_{cr}=N_a/\eta$ may also be expressed in terms of the monocoque buckling coefficient P, substituting the value of η from equation (8.38) results in

$$P_{cr}=\frac{Pe}{\eta}=\frac{Pe}{1+\dfrac{20.7P(E_{1_t}t_1+E_{2_t}t_2)}{\lambda^42G_cR}} \tag{8.39}$$

Equation (8.39) has been plotted in figure 8.1 to show the variation of the buckling parameter P as a function of the shear stiffness of the core. The basic monocoque curve was based upon data using a 90 percent probability curve.

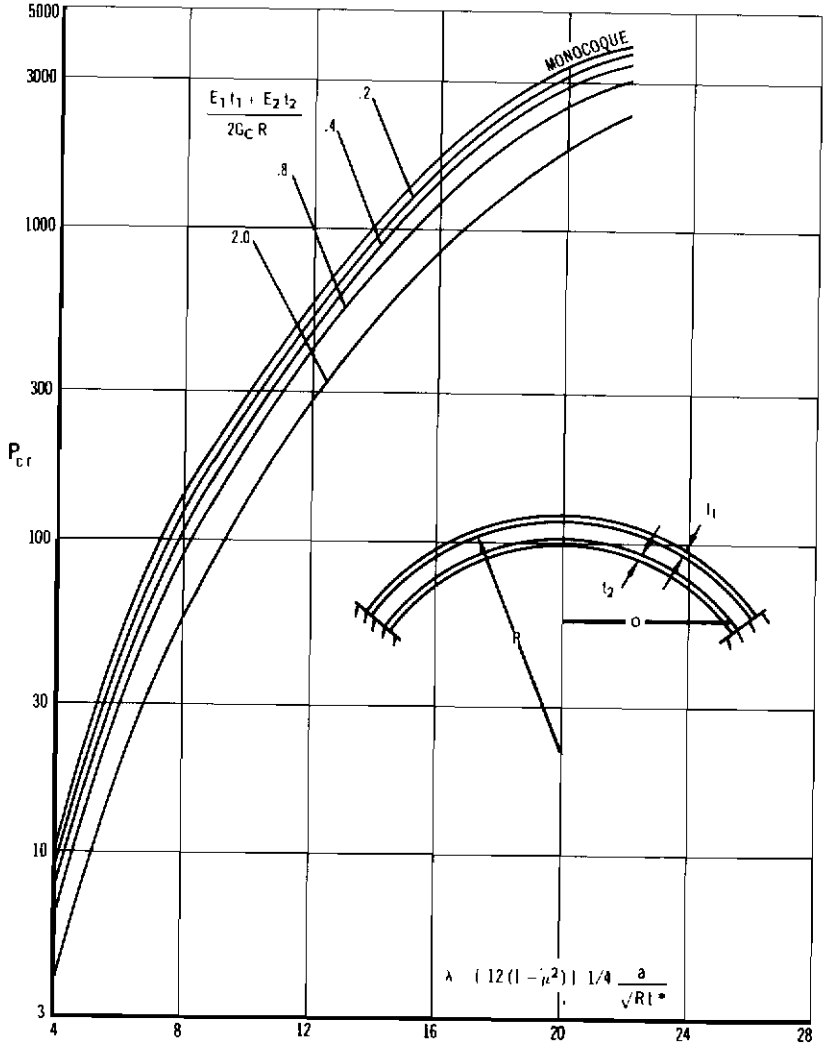

FIGURE 8.1—Buckling of sandwich spherical caps under external pressure.

Example Problem

Spherical radius, $R=80$ in.
Base radius, $a=100$ in.
Face material, 2014–T6 aluminum alloy
Core material, HRP 3/16—4 lb/ft^3
$t_c=2.00$ in.
$t_1=0.020$ in.
$t_2=0.040$ in.
$G_c=12\ 000$ lbs/in.^{2}

Outer face t_1 is at $-423°$ F
Inner face t_2 is at room temperature
$\mu=0.30$

Neglecting thermal gradient stress, find the critical buckling pressure q_{cr}.

From equation (8.15) compute t^*, assuming elastic modulus values of $E_{1_s}=12.3\times10^6$ and $E_{2_s}=10.5\times10^6$, where

$$t^*=\frac{1.73}{E_{1_s}t_1+E_{2_s}t_2}\frac{\sqrt{(E_{1_s}t_1+E_{2_s}t_1)E_{1_s}t_1\left[(2t-t_1)^2+\dfrac{E_{2_s}t_2^3}{E_{1_s}t_1}\right]}}{-[E_{1_s}t_1(2t-t_1)+E_{2_s}t_2^2]^2}$$

Substituting the assumed elastic secant moduli for E_{1_s} and E_{2_s} at temperature from figure 8.2, and the value of t_1, t_2, and t into the above equation results in $t^*=3.39$.

From equation (8.14) compute the parameter λ, where

$$\lambda=[12(1-\mu^2)]^{1/4}\frac{a}{\sqrt{Rt^*}}$$

This results in $\lambda=11.1$.

Compute the parameter $(E_{1_t}t_1+E_{2_t}t_2)/(2RG_c)$ from figure 8.1, where E_{1_t} and E_{2_t} are the elastic tangent modulus values. This gives

$$\frac{12.3\times10^6\times.02+10.5\times10^6\times.04}{2\times80\times12\times10^3}=0.347$$

From the curve in figure 8.2 reading in the appropriate computed values gives $P_{cr}=360$.

Since the buckling parameter P_{cr} may yield membrane stresses above the proportional limit of the facing material, it is recommended that the buckling stresses be computed before the critical buckling pressure.

From equation (8.29)

$$P_{cr}=\frac{2(1-\mu^2)a^4\sigma_{2,}\,\sigma_1}{t^{*3}RE_{2_t}E_{1_t}}$$

or this may be written as

$$A=\frac{\sigma_2}{E_{2_t}}=\frac{\sigma_1}{E_{1_t}}=\frac{Pt^{*3}R}{2(1-\mu^2)a^4}$$

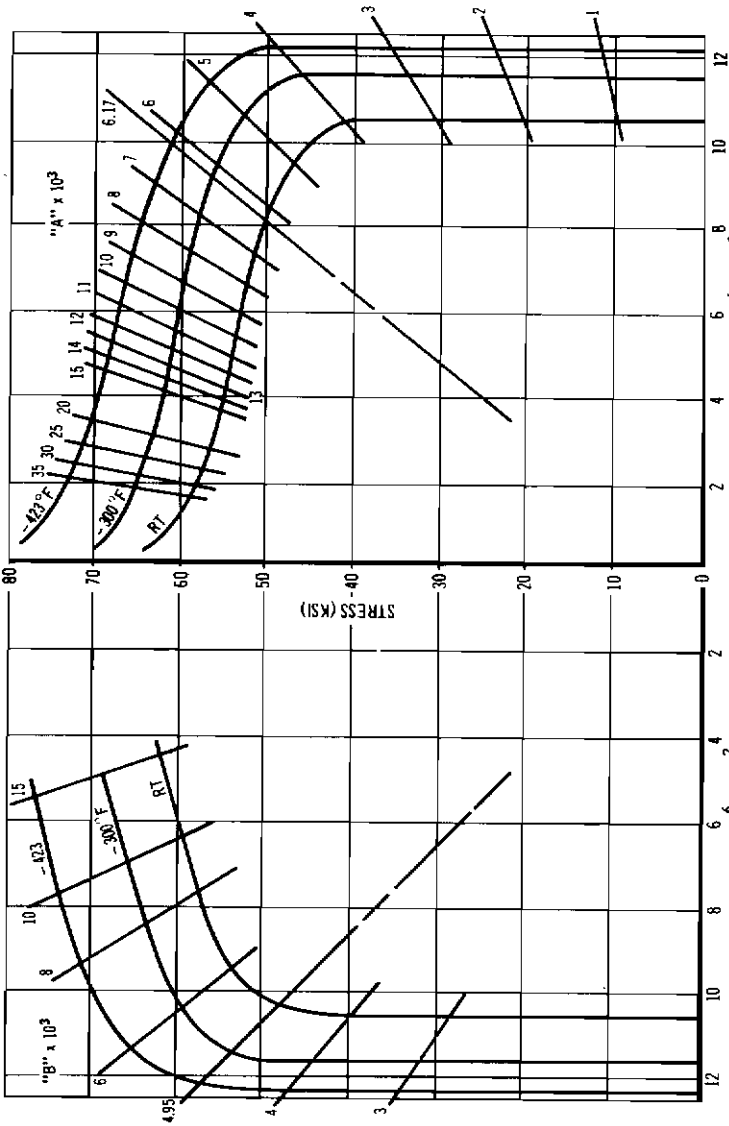

FIGURE 8.2—Compression tangent modulus curve for 2014-T6 aluminum.

Various A values have been constructed in figure 8.2. Substituting the values of P_{cr}, t^*, R, and a into the above equation results in

$$A=\frac{360\times(3.39)^3 80}{2(1-0.3^2)100^4}$$

$$A=6.17\times10^{-3}$$

This value of A described in figure 8.2 shows that the predicted stress is above the proportional limit of the facing materials; therefore, an iterative approach must be used to arrive at a solntion. At $A=6.17\times10^{-3}$, the stresses in the faces from figure 7.14 are

$$\sigma_1=61\ 500 \text{ psi at } E_{1_t}=10\times10^6$$

and

$$\sigma_2=51\ 000 \text{ psi at } E_{2_t}=8.25\times10^{-6}$$

The appropriate secant moduli at these stresses are

$$E_{1_s}=12.1\times10^6,\ E_{2_s}=10.3\times10^6$$

Substituting the above values of E_{1_s} and E_{2_s} into equation (8.15) for t* results in

$$t^*=3.39$$

which is the same value as originally calculated.

Since the value of t^* is the same, and from equation (8.14) the value of λ is a function of the variable t^*, therefore $\lambda=11.1$.

Recomputing the parameter $(E_{1_t}t_1+E_{2_t}t_2)/(2RG_c)$ using $E_{1_t}=10\times10^6$ and $E_{2_t}=8.25\times10^6$ from the first calculation results in the value of 0.276. From figure 8.1, $P_{cr}=360$.

Since t^* and P_{cr} remain the same, the computed value of A is also the same. Therefore, for this particular example, a solution has been determined that satisfies the original values of the secant moduli.

To establish the buckling pressure it must be stated that, unlike a solution in the elastic region where both faces presumably fail together, the plastic region results in one face with the minimnm strain failing first. Therefore, to determine the actual failing pressure, it is necessary to determine this minimum strain. This can best be accomplished by the following method

At the A value of 6.17×10^{-3}, the corresponding B values or strains result in $B_2<B_1$. Since the strains must be equal in the faces, it

follows that a solution exists at the minimum strain value at B_2. Therefore constructing the B_2 line in figure 8.2 where

$$B_2=\frac{\sigma_2}{E_{2_s}}=\frac{51\,000}{10.3\times10^6}=4.95\times10^{-3}$$

and at the intersection of the outer face at $-423°$ F, results in

$$\sigma_1=60\,000 \text{ lb/in.}^2$$

The allowable buckling pressure is, therefore,

$$\sigma_1 t_1+\sigma_2 t_2=\frac{qR}{2}$$

or

$$q=\frac{2}{80}[60\times10^3\times0.02+51\times10^3\times0.04]$$

$$q=81 \text{ lb/in.}^2$$

CHAPTER 9

The Tensile Paradox

IN CERTAIN ELLIPTICAL DOMES or segments of a truncated sphere, the application of internal pressure will paradoxically produce a compressive hoop stress which may result in a compressive buckling failure of the shell, even though the shell is primarily under tension. Figure 9.1 shows a compressive buckling failure on a truncated segment of a sphere. A uniform tension load was applied at the periphery of the truncated segment. Because theory for this latter failure is not well represented in the literature, a solution will be offered here.

A theory of *local instability* is developed along the lines of the book, *Non-Linear Theory of Thin Elastic Shells*,[1] edited by Mushtari and Galimov, from the approximate equations of compatibility and equilibrium (equations 57.5 and 57.6 in the book):

$$\Delta\Delta\psi-\frac{Et}{R_1R_2}\left(\frac{1}{R_1}w_{\theta\theta}+\frac{1}{R_2\sin^2\theta}w_{\beta\beta}\right)=0 \tag{9.1}$$

$$\Delta\psi=\frac{1}{R_1^2}\psi_{\theta\theta}+\frac{1}{R_2^2\sin^2\theta}\psi_{\beta\beta}$$

$$D\Delta\Delta w+\frac{1}{R_1R_2^2\sin^2\theta}\psi_{\beta\beta}+\frac{1}{R_1^2R_2}\psi_{\theta\theta}-\frac{T_1^I}{R_1^2}w_{\theta\theta}-\frac{T_2^I}{R_2^2\sin^2\theta}w_{\beta\beta}=0 \tag{9.2}$$

It will be sbown at a later stage of this analysis that the assumption of a large number of buckles can be predicted by the theory and substantiated by the test results. In fact, the actual buckled configuration has been used as a guide to reduce the number of independent variables from two to one. The number of buckles will be computed to ensure the validity of the equations and this number will be compared with the actual number as determined by test. The spherical shell segment as shown is loaded by tangential tensile loads at points a and b which are radially restrained. A single buckle forms between a and b and is repeated a considerable number of times around the circumference.

[1] Mushtari, Kh. M., and Galimov, K. Z., editors: *Non-Linear Theory of Thin Elastic Shells.* Academy of Sciences, USSR, 1957.

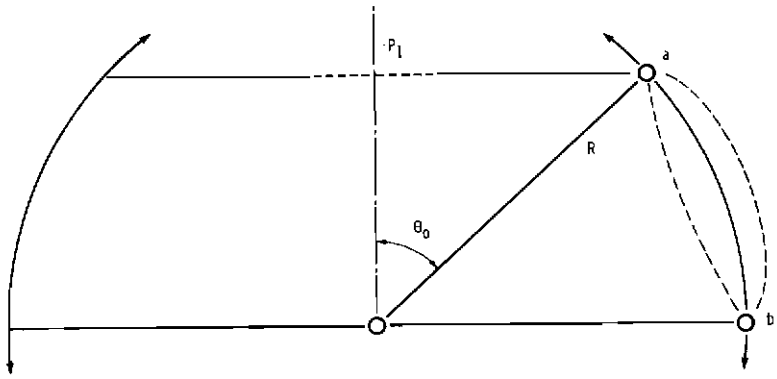

FIGURE 9.1—Observed buckle configuration.

In order to pass through points a and b, the radial deflection function

$$w=C \sin m(\theta-\theta_0) \cos n\beta$$

must be chosen such that $m(\pi-2\theta_0)=2\pi$, giving

$$m_1=\frac{m}{R}=\left(\frac{2\pi}{\pi-2\theta_0}\right)\left(\frac{1}{R}\right)$$

The expression derived for P_1 which is to be minimized with respect to n is

$$P_1 \frac{\sin^2 \theta_0}{\sin^2 \theta}=D \frac{(m_1^2+n_1^2)^2}{n_1^2-m_1^2}+\frac{Et}{R^2}\frac{1}{n_1^2-m_1^2} \tag{9.3}$$

In order to facilitate the work, the following expressions will be defined

$$\left.\begin{aligned} m_1^2&=\left(\frac{2\pi}{\pi-2\theta_0}\right)^2\frac{1}{R^2}=a \\ n_1^2&=x \\ \frac{Et}{DR^2}&=\alpha \end{aligned}\right\} \tag{9.4}$$

Utilizing equation (9.4), equation (9.3) becomes

$$P_1 \frac{\sin^2 \theta_0}{D \sin^2 \theta}=\frac{(a+x)^2}{x-a}+\frac{\alpha}{x-a} \tag{9.5}$$

The expression on the left-hand side is to be minimized with respect to x. Therefore,

$$\left(P_1 \frac{\sin^2 \theta_0}{\sin^2 \theta}\times\frac{1}{D}\right)_x=\frac{(x-a)(2)(x+a)-[(x+a)^2+\alpha]}{(x-a)^2}$$

$$=\frac{x^2-2ax-(3a^2+\alpha)}{(x-a)^2}=0$$

giving

$$x=a\left(1\pm\sqrt{4+\frac{\alpha}{a^2}}\right)=n_1^2$$

But $n_1^2>0$, hence the positive sign must be chosen, and

$$x=a\left(1+\sqrt{4+\frac{\alpha}{a^2}}\right) \tag{9.6}$$

To assure that this does yield a *minimum*, further differentiation yields

$$\left(P_1\frac{\sin^2\theta_0}{\sin^2\theta}\cdot\frac{1}{D}\right)_{xx}=\frac{2}{\sqrt{4a^2+\alpha}}>0$$

Thus, equation (9.6) is the required value of x (or n_1^2), to obtain minimal load conditions for P_1.

Equation (9.6) may also be used to obtain the number of buckles. Define the quantities

$$\gamma=\left(\frac{2\pi}{\pi-2\theta_0}\right)^2,\ b^2=3(1-\nu^2),\ \rho=\frac{R}{t}$$

then

$$a=\frac{\gamma}{R^2}$$

$$\frac{\alpha}{a^2}=\frac{Et}{DR^2}\frac{R^4}{\gamma^2}=\frac{EtR^2}{\gamma^2}\cdot\frac{12(1-\nu^2)}{Et^3}=\frac{4b^2\rho^2}{\gamma^2}$$

$$x=n_1^2=\left(\frac{n}{R\sin\theta}\right)^2=\frac{\gamma}{R^2}\left(1+\sqrt{4+\frac{4b^2\rho^2}{\gamma^2}}\right)$$

giving the buckle number, n, as

$$n^2=\gamma\sin^2\theta\left(1+2\sqrt{1+b^2\left(\frac{\rho}{\gamma}\right)^2}\right) \tag{9.7}$$

In order to substitute equation (9.6) into (9.5) and determine P_1 (min), we first determine

$$x-a=a\sqrt{4+\frac{\alpha}{a^2}}=\frac{2\gamma}{R^2}\sqrt{1+\frac{b^2\rho^2}{\gamma^2}}$$

$$x+a=2a\left(1+\sqrt{1+\frac{\alpha}{4a^2}}\right)=\frac{2\gamma}{R^2}\left(1+\sqrt{1+\frac{b^2\rho^2}{\gamma^2}}\right)$$

Now define

$$\frac{b^2\rho^2}{\gamma^2}=y$$

giving

$$x-a=\frac{2\gamma}{R^2}\sqrt{1+y},\ x+a=\frac{2\gamma}{R^2}(1+\sqrt{1+y}) \tag{9.8}$$

Substituting equation (9.8) into (9.5), and observing that the maximum buckling stresses occur at $\theta=\theta_0$, then

$$\frac{P_1}{D}=\frac{\frac{4\gamma^2}{R^4}(1+\sqrt{1+y})^2}{\frac{2\gamma}{R^2}\sqrt{1+y}}+\frac{Et}{R^2}\frac{12(1-\nu^2)}{Et^3}\frac{1}{\frac{2\gamma}{R^2}\sqrt{1+y}}$$

$$=\frac{2\gamma}{R^2}\frac{(1+\sqrt{1+y})^2}{\sqrt{1+y}}+\frac{2b^2}{\gamma t^2}\frac{1}{\sqrt{1+y}}$$

But,

$$\frac{P_1}{D}=\frac{P_1}{Et^3}12(1-\nu^2)=\frac{4b^2p_1}{Et^3}$$

giving

$$\frac{P_1}{Et}=\frac{\gamma}{2R^2}\frac{t^2}{b^2}\frac{(1+\sqrt{1+y})^2}{\sqrt{1+y}}+\frac{b^2}{2\gamma t^2}\frac{t^2}{b^2}\frac{1}{\sqrt{1+y}}$$

$$=\frac{\gamma}{2b^2\rho^2}\frac{(1+\sqrt{1+y})^2}{\sqrt{1+y}}+\frac{1}{2\gamma}\frac{1}{\sqrt{1+y}}$$

$$=\frac{1}{2\gamma y}\frac{(1+\sqrt{1+y})^2}{\sqrt{1+y}}+\frac{1}{2\gamma}\frac{1}{\sqrt{1+y}}$$

since

$$\frac{\gamma^2}{b^2\rho^2}=\frac{1}{y}$$

Now define $\sqrt{1+y}=Z$, $y=Z^2-1$, giving

$$\frac{P_1}{Et}=\frac{1}{2\gamma Z}\left[\frac{(1+Z)^2}{Z^2-1}+1\right]=\frac{1}{2\gamma Z}\frac{2Z^2+2Z}{Z^2-1}$$

$$\frac{P_1}{Et}=\frac{1}{\gamma}\cdot\frac{1}{Z-1}=\frac{1}{\gamma}\cdot\frac{1}{\sqrt{1+y}-1} \tag{9.9}$$

since $Z+1\neq 0$.

Equation (9.9) is brought into its clearest form when expanded by the binomial theorem. The expansion will be made in powers of $1/y$ since y is large.

$$\frac{P_1}{Et}=\frac{1}{\gamma}\frac{1}{y^{1/2}\sqrt{1+\frac{1}{y}}-1}$$

$$=\frac{1}{\gamma}\frac{1}{\frac{b\rho}{\gamma}\left[1+\frac{1}{2}\left(\frac{\gamma^2}{b^2\rho^2}\right)+\frac{(1/2)(-1/2)}{2!}\left(\frac{\gamma^2}{b^2\rho^2}\right)^2+\ldots\right]-1}$$

where, for $\nu=0.3$, $b^2=3(1-\nu^2)=2.73$, and $b=1.652$. Thus,

$$\frac{P_1}{Et}=\frac{1}{1.652\rho\left[1+\frac{1}{5.46}\left(\frac{\gamma}{\rho}\right)^2-\frac{1}{59.5}\left(\frac{\gamma}{\rho}\right)^4+\ldots\right]-\gamma}$$

$$\frac{P_1R}{Et^2}=\frac{1}{1.652\left[1+\frac{1}{5.46}\left(\frac{\gamma}{\rho}\right)^2-\frac{1}{59.5}\left(\frac{\gamma}{\rho}\right)^4+\ldots\right]-\frac{\gamma}{\rho}}$$

giving, finally,

$$\frac{P_1R}{Et^2}=C\left(\frac{\gamma}{\rho}\right)=\frac{0.606}{1-\frac{1}{1.652}\left(\frac{\gamma}{\rho}\right)+\frac{1}{5.46}\left(\frac{\gamma}{\rho}\right)^2-\frac{1}{59.5}\left(\frac{\gamma}{\rho}\right)^4+\ldots} \tag{9.10}$$

for the buckling edge load, P_1, and

$$n^2=\gamma\sin^2\theta_0\left[1+2\sqrt{1+2.73\left(\frac{\rho}{\gamma}\right)^2}\right] \tag{9.11}$$

for the number of buckles, n. Since the buckles should initiate at the small end, θ_0 is used.

It will be observed that γ/ρ increases as θ_0 and t increase, which means that larger buckling values are obtained for close-truncated thick specimens. In fact, equation (9.9) shows that P_1 is monotonically increasing, and approaches infinity for large values of γ/ρ since $y\to 0$ when $\gamma/\rho\to\infty$. Such geometries are approaching that of a tensile test specimen in the same manner that short thick Euler columns are approaching that of a compressive test specimen.

Equation (9.10) is to be interpreted as a "classical" result obtained from linear theory and as not including the effects of imperfections. Similar classical values, using equations (9.1) and (9.2), have been obtained for the sphere under external pressure, the end loaded cylinder, and the cylinder under hydrostatic pressure. These three cases provide additional verification of equations (9.1) and (9.2).

Just as in almost every other shell buckling solution, actual design allowables must be obtained and justified by test. The effects of nonlinearity, imperfections and test methods, all of which can have

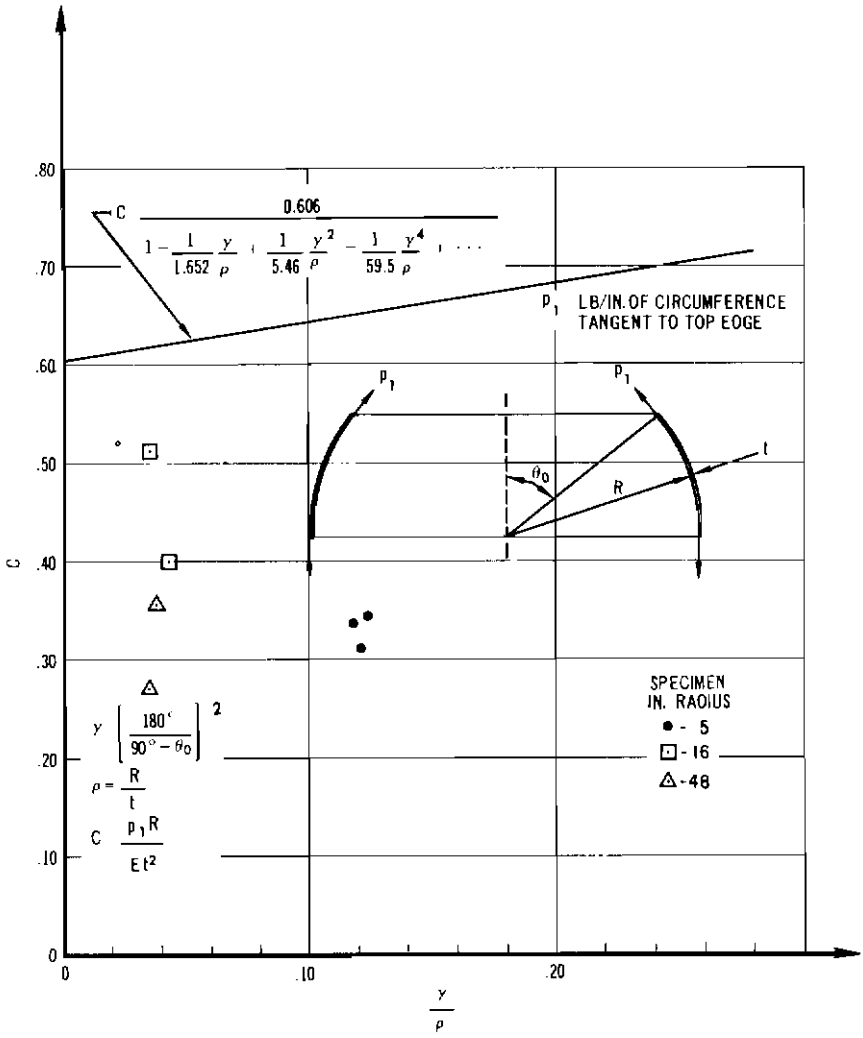

FIGURE 9.2—Test values of C vs γ/ρ.

significant influence upon the actual test values, are not readily incorporative in the theory. This is the situation in general and this report is no exception to the general rule.

Test values are reproduced as a graph of C versus γ/ρ in figure 9.2. It is to be noted that more scatter is to be expected in the low γ/ρ values, since imperfections have more influence upon thin than upon thick specimens for a given radius. Design allowables based upon a statistical probability exception from these seven tests are not recommended since the wide scatter in these few tests would result in exces-

sively low C values and impose undue penalties upon the designer. It is recommended that further testing be undertaken. However, until additional values can be obtained, a C not greater than the minimum, $C=0.273$, should be employed.

A final remark regarding the test values is in order. The buckling test loads noted are those given at the instant of the first buckle formation. Additional loading results in more complete buckle patterns at considerably higher loads.

The number of buckles will now be computed to verify the assumption that a large number of buckles are formed. First, however, a close approximation to equation (9.11) will be derived. Since

$$2.73\left(\frac{\rho}{\gamma}\right)^2 >> 1$$

we may write

$$n^2=\gamma \sin^2 \theta_0\left[1+2\sqrt{2.73}\left(\frac{\rho}{\gamma}\right)\right]$$

If, in addition,

$$2\sqrt{2.73}\left(\frac{\rho}{\gamma}\right) >> 1$$

we obtain

$$n=1.82\sqrt{\rho}\sin\theta_0 \tag{9.12}$$

TABLE 9.1—Approximate n Values From Calculation and Test

Spec.	γ	ρ	$\frac{\rho}{\gamma}$	Value of n		
				From (9.10)	From (9.9)	Approx., as measured *
1	57.6	481	8.35	36.6	37.3	30
2	57.6	477	8.27	36.4	37.2	30
3	57.6	454	7.88	35.6	35.7	30
4	27.3	759	27.8	41.3	41.6	28
5	27.3	638	23.4	37.9	38.2	30
6	57.6	1600	27.8	66.8	67.2	50
7	57.6	1510	26.2	64.8	65.3	35

* Only approximate n values as measured from tests could be obtained, since complete buckle patterns were not formed in some cases, and in others, estimates had to be made from photographs.

U.S. GOVERNMENT PRINTING OFFICE: 1964 O—769-377